

Attenuation imaging by wavefield reconstruction inversion with bound constraints and total variation regularization

Hossein S. Aghamiry^{1,2}, Ali Gholami¹ and Stéphane Operto²

ABSTRACT

Wavefield reconstruction inversion (WRI) extends the search space of Full Waveform Inversion (FWI) by allowing for wave equation errors during wavefield reconstruction to match the data from the first iteration. Then, the wavespeeds are updated from the wavefields by minimizing the source residuals. Performing these two tasks in alternating mode breaks down the nonlinear FWI as a sequence of two linear subproblems, relying on the bilinearity of the wave equation. We solve this biconvex optimization with the alternating-direction method of multipliers (ADMM) to cancel out efficiently the data and source residuals in iterations and stabilize the parameter estimation with appropriate regularizations. Here, we extend WRI to viscoacoustic media for attenuation imaging. Attenuation reconstruction is challenging because of the small imprint of attenuation in the data and the cross-talks with velocities. To address these issues, we recast the multivariate viscoacoustic WRI as a triconvex optimization and update wavefields, squared slowness, and attenuation factor in alternating mode at each WRI iteration. This requires to linearize the attenuation-estimation subproblem via an approximated trilinear viscoacoustic wave equation. The iterative defect correction embedded in ADMM corrects the errors generated by this linearization, while the operator splitting allows us to tailor ℓ_1 regularization to each parameter class. A toy numerical example shows that these strategies mitigate cross-talk artifacts and noise from the attenuation reconstruction. A more realistic synthetic example representative of the North Sea validates the method.

INTRODUCTION

Full waveform inversion (FWI) is a high-resolution nonlinear imaging technology which can provide accurate subsurface model by matching observed and calculated waveforms (Tarantola, 1984; Pratt et al., 1998; Virieux and Operto, 2009). However, it is well acknowledged that it suffers from two main pathologies. The first one is the nonlinearity associated with cycle skipping: When the distance between the observed and calculated data is the least-squares norm of their differences, FWI remains stuck into spurious local minima when the initial velocity model does not allow to match traveltimes with an error lower than half a period. To mitigate cycle skipping, many variants of FWI have been proposed with more convex distances such as those based on matching filters (Warner and Guasch, 2016; Guasch et al., 2019) or optimal transport (Métivier et al., 2018) among others. The second pathology is ill-posedness resulting from uneven subsurface illumination provided by limited-aperture surface acquisitions (e.g., Tang, 2009) and parameter cross-talks during multiparameter reconstruction (see Operto et al., 2013, for a tutorial). Mitigating this ill-posedness requires to account for the Hessian in local optimization methods (e.g. Métivier et al., 2017) and regularize the inversion with prior information such as physical bound constraints (e.g. Asnaashari et al., 2013; Duan and Sava, 2016).

Among the methods proposed to mitigate cycle skipping, wavefield reconstruction inversion (WRI) (van Leeuwen and Herrmann, 2013, 2016) extends the parameter search space of frequency-domain FWI by processing the wave equation as a soft constraint with a penalty method. The resulting wave equation relaxation allows for data fitting with inaccurate velocity models through the reconstruction of data-assimilated wavefields, namely wavefields satisfying the observation equation relating the wavefields to the observations (Aghamiry et al., 2019a). The algorithm then updates the model parameters by least-squares minimization of the wave equation errors (or source residu-

⁰ ¹University of Tehran, Institute of Geophysics, Tehran, Iran, email: h.ghamiry@ut.ac.ir, agholami@ut.ac.ir

²University Cote d'Azur - CNRS - IRD - OCA, Geoazur, Valbonne, France, email: aghamiry@geoazur.unice.fr, operto@geoazur.unice.fr

als) so that the assimilated wavefields explain both the wave equation and the data as well as possible. Performing wavefield reconstruction and parameter estimation in an alternating mode (van Leeuwen and Herrmann, 2013) rather than by variable projection (van Leeuwen and Herrmann, 2016) recasts WRI as a sequence of two linear subproblems as a result of the bilinearity of the wave equation in wavefield and squared slowness. The reader is also referred to Aghamiry et al. (2019b) for a more general discussion on the bilinearity of the elastic anisotropic wave equation. Aghamiry et al. (2019e) solved this bi-convex problem with the alternating direction method of multipliers (ADMM) (Boyd et al., 2010). ADMM is an augmented Lagrangian method which makes use of operator splitting and alternating directions to solve convex separable multi-variate constrained problems. The augmented Lagrangian function combines a penalty function and a Lagrangian function (Nocedal and Wright, 2006a, Chapter 17). The penalty function relaxes the constraints during early iterations as in WRI, while the Lagrangian function progressively corrects the constraint violations via the action of the Lagrange multipliers. The leverage provided by the Lagrange multipliers guarantees to satisfy the constraints at the convergence point with constant penalty parameters (Aghamiry et al., 2019e). Accordingly, Aghamiry et al. (2019e) called their approach iteratively-refined WRI (IR-WRI). Alternatives to satisfy the constraints at the convergence point with penalty methods rely on multiplicative (da Silva and Yao, 2017) or discrepancy-based (Fu and Symes, 2017) approaches. Aghamiry et al. (2019d) implemented bounding constraints and total variation (TV) regularization (Rudin et al., 1992) in IR-WRI with the split Bregman method (Goldstein and Osher, 2009) to improve the imaging of large-contrast media, with however undesirable staircase imprints in smooth regions. To overcome this issue and capture both the blocky and smooth components of the subsurface, Aghamiry et al. (2019c) combine in IR-WRI Tikhonov and TV regularizations by infimal convolution.

The objective of this paper is to extend frequency-domain IR-WRI to viscoacoustic media for attenuation imaging. Attenuation reconstruction by FWI raises two potential issues. The first is related to the cross-talks between wavespeed and attenuation. The ambiguity between velocity and attenuation perturbation in least-squares migration has been emphasized by Mulder and Hak (2009). Many combination of velocity and attenuation perturbations can fit equally well reflection amplitudes since they are basically related by an Hilbert transform. This ambiguity can be simply illustrated by the radiation pattern of velocity and attenuation perturbations, which have the same amplitude versus angle behavior and a 90° phase shift (Malinowski et al., 2011; da Siva et al., 2019). The conclusions of Mulder and Hak (2009) are substantiated by Ribodetti et al. (2000) who show that the Hessian of ray+Born least-squares migration of single-offset reflection data is singular if the reflector is not illuminated from

above and beneath. On the other hand, Hak and Mulder (2011) show that wavespeed and attenuation can be decoupled during nonlinear waveform inversion of multi-offset/multi-frequency data provided that the causality term is properly implemented in the attenuation model. This conclusion has been further supported by several realistic synthetic experiments and real data case studies in marine and land environments, which manage to reconstruct trustworthy attenuation models (Hicks and Pratt, 2001; Askan et al., 2007; Malinowski et al., 2011; Takougang and Calvert, 2012; Kamei and Pratt, 2008; Prieux et al., 2013; Stopin et al., 2016; Operto and Miniussi, 2018; Lacasse et al., 2019). This decoupling between velocity and attenuation can be further argued on the basis of physical considerations. In the transmission regime of wave propagation, wavespeeds control the kinematic of wave propagation. This implies that FWI is dominantly driven toward wavespeed updating to match the traveltimes of the wide-aperture data (diving waves, post-critical reflections) and update the long wavelengths of the subsurface accordingly, while attenuation has a secondary role to match amplitude and dispersion effects (e.g., see Operto and Miniussi, 2018, for an illustration). This weak imprint of the attenuation in the seismic response was illustrated by the sensitivity analysis carried out by Kurzman et al. (2013) who concluded that a crude homogeneous background attenuation model may be enough to perform reliable FWI, while da Siva et al. (2019) proposed to reconstruct an under-parametrized attenuation model by semi global FWI. When a high-resolution attenuation model is sought, the ill-posedness of the attenuation reconstruction may be managed with different recipes including data-driven and model-driven inversions (joint versus sequential updates of the velocity and attenuation of selected subdatasets), parameter scaling, bound constraints and regularizations (e.g. Prieux et al., 2013; Operto et al., 2013).

In this context, the contribution of this study is two fold: first, we show how to implement velocity and attenuation reconstruction in frequency-domain viscoacoustic IR-WRI when equipped with bound constraints and nonsmooth regularizations. Second, we discuss with numerical examples whether the alternating-direction algorithm driven by the need to expand the search space is suitable to manage ill-conditioned multi-parameter reconstruction. It is well acknowledged that viscous effects are easily included in the time-harmonic wave equation with frequency-dependent complex-valued velocities as function of phase velocity and attenuation factor (the inverse of quality factor) which are both real-valued parameters (Toksöz and Johnston, 1981). Accordingly, the objective function of viscoacoustic IR-WRI requires to be minimized over a set of three parameter classes (wavefield, squared slowness, attenuation factor). In this study, we consider the Kolsky-Futterman model as attenuation model (Kolsky, 1956; Futterman, 1962). With this model, the viscoacoustic wave equation is bilinear in wavefield and squared slowness, while it is

nonlinear in attenuation factor. This prompts us to introduce a first-order approximation of the viscoacoustic function to form a trilinear viscoacoustic wave equation. This equation allows us to recast the multivariate viscoacoustic IR-WRI as a sequence of three linear subproblems for wavefields, squared slowness and attenuation factor estimation, which are solved in alternating mode following the block relaxation strategy of ADMM. Then, the errors generated by the approximated wave equation during attenuation estimation are corrected by the action of the Lagrange multipliers (dual variables), which are formed by the source residuals computed with the exact wave equation. Another application of augmented Lagrangian method in AVO inversion is presented in Gholami et al. (2018) where the linearized Zoeppritz equations are used to simplify the primal problem, while the dual problem compensates the linearization-related errors by computing the residuals with the exact Zoeppritz equations. Also, the decomposition of the viscoacoustic IR-WRI into three linear subproblems provides the suitable framework to tailor ℓ_1 regularizations to each parameter-estimation subproblem (Aghamiry et al., 2019d,c).

The alternating update of the squared slowness and attenuation factor at each IR-WRI iteration is probably non neutral on how the inversion manages the parameter cross-talks and the contrasted sensitivity of the data to each parameter class, as the multi-parameter inversion is broken down as a sequence of two mono-parameter inversions. This approach differs from those commonly used in multi-parameter inversion. The most brute-force approach consists in the joint updating of the multiple parameter classes, with the issue of managing multi-parameter Hessian with suitable parameter scaling (e.g., Stopin et al., 2014; Métivier et al., 2015; Yang et al., 2016). Other approaches rely on ad-hoc hierarchical data-driven and model-driven inversion where the dominant parameter is updated during a first mono-parameter inversion, before involving the secondary parameter in a subsequent multi-parameter inversion (e.g., Prioux et al., 2013; Cheng et al., 2016). Another possible model-driven strategy consists of performing the joint updating of the multiple parameter classes during a first inversion, then reset the secondary parameters to their initial values and restart a multi-parameter inversion involving all the parameter classes (Yang et al., 2014).

In this study, we assess our approach against two synthetic experiments, a toy example and a more realistic well-documented synthetic example representative of the North Sea (Prioux et al., 2013). A comparison of our approach with those reviewed above remains however beyond the scope of this paper. One reason is that all the above approaches have been implemented in conventional FWI, which would remain stuck in a local minimum when starting from the crude initial model used in this study. This is to remind that IR-WRI provides a practical framework to conciliate the search space expansion to mitigate cycle skipping and easy-to-design multi-parameter recon-

struction via the alternating update of the multiple parameter classes.

This paper is organized as follow. In the method section, we first review the forward problem equation before going into the details of viscoacoustic IR-WRI: We first formulate the constrained optimization problem to be solved and recast it as a saddle point problem with an augmented Lagrangian function (Appendix A). Then, we review the solution of the three primal subproblems for wavefields, squared slowness and attenuation factor in the framework of ADMM, as well as the expression of the dual variables or Lagrange multipliers that capture the history of the solution refinement in iterations. The appendix B reviews in a general setting the split Bregman method to solve ℓ_1 -regularized convex problem. This recipe can be easily applied to the squared slowness and attenuation reconstruction subproblems. The final section presents two synthetic examples, which are performed without and with bound constraints and TV regularization in order to discriminate the role of the augmented-Lagrangian optimization from that of the priors. A toy example allows us to illustrate in a simple setting how well IR-WRI manages the parameter cross-talk and the ill-posedness of the attenuation reconstruction and how bound constraints and TV regularization remove the corresponding artifacts. A second synthetic example representative of the North Sea environment allows one to assess the method in a more realistic setting.

THEORY

In this section, we first review the viscoacoustic wave equation in the frequency-space domain. Then, we use this wave equation to formulate the iteratively-refined wavefield reconstruction inversion (IR-WRI) for velocity and attenuation.

Forward problem

The viscoacoustic wave equation in the frequency-space domain is given by

$$\left(\Delta + \frac{\omega^2}{c(\mathbf{x})^2}\right) u(\mathbf{x}, \omega) = b(\mathbf{x}, \omega), \quad (1)$$

where Δ is the Laplacian operator, ω is the angular frequency, $\mathbf{x} = (x, z)$ denotes the position in the subsurface model and $b(\mathbf{x}, \omega)$ and $u(\mathbf{x}, \omega)$ are respectively the source term and the wavefield for frequency ω . Viscoacoustic (attenuative) media can be described by complex-valued velocity $c(\mathbf{x})$. The velocity associated with the Kolsky-Futterman model is given by (Kolsky, 1956; Futterman, 1962)

$$\frac{1}{c(\mathbf{x})} = \frac{1}{v(\mathbf{x})} \left[1 - \frac{1}{\pi Q(\mathbf{x})} \log \left| \frac{\omega}{\omega_r} \right| + i \frac{\text{sign}(\omega)}{2Q(\mathbf{x})} \right], \quad (2)$$

where $v(\mathbf{x})$ denotes the phase velocity, $Q(\mathbf{x})$ the frequency-independent quality factor, both real-valued, and $i = \sqrt{-1}$.

Also, $\text{sign}(\bullet)$ is the sign function that extracts the sign of a real number \bullet . The logarithmic term with reference frequency $\omega_r = 2\pi f_r$ implies causality (Aki and Richards, 2002; Hak and Mulder, 2011). In this study, f_r is chosen to be 50 Hz (Toverud and Ursin, 2005).

Inverse problem

We discretize the 2D partial-differential equation (PDE), equation 1, with a $N = N_x \times N_z$ grid points, where N_x and N_z are the number of points in the horizontal and vertical directions, respectively. We parametrize the inversion by squared slowness $m = 1/v^2$ and attenuation factor $\alpha = 1/Q$. Accordingly, equation 2 in discrete form reads as

$$\frac{1}{\mathbf{c}^2} = \mathbf{m} \circ \rho(\boldsymbol{\alpha}), \quad (3)$$

where

$$\rho(\alpha) = (1 + \beta(\omega)\alpha)^2, \quad \beta(\omega) = i \frac{\text{sign}(\omega)}{2} - \frac{1}{\pi} \log \left| \frac{\omega}{\omega_r} \right| \quad (4)$$

and \circ denotes Hadamard (element wise) product operator.

The model parameters $\mathbf{m} \in \mathbb{R}^N$ and $\boldsymbol{\alpha} \in \mathbb{R}^N$ are defined as solution of the following nonlinear PDE-constrained optimization problem (Aghamiry et al., 2019e)

$$\begin{aligned} & \min_{\mathbf{u}, \mathbf{m} \in \mathcal{M}, \boldsymbol{\alpha} \in \mathcal{A}} \quad \mu E(\mathbf{m}) + \nu F(\boldsymbol{\alpha}) \\ & \text{subject to} \quad \begin{cases} \mathbf{A}(\mathbf{m}, \boldsymbol{\alpha})\mathbf{u} = \mathbf{b} \\ \mathbf{P}\mathbf{u} = \mathbf{d}, \end{cases} \end{aligned} \quad (5)$$

where $\mathbf{u} \in \mathbb{C}^{N \times 1}$ is the wavefield, $\mathbf{b} \in \mathbb{C}^{N \times 1}$ is the source term, and $\mathbf{A}(\mathbf{m}, \boldsymbol{\alpha}) \in \mathbb{C}^{N \times N}$ is the matrix representation of the discretized Helmholtz PDE, equation 1. The observation operator $\mathbf{P} \in \mathbb{R}^{M \times N}$ samples the reconstructed wavefields at the M receiver positions for comparison with the recorded data $\mathbf{d} \in \mathbb{C}^{M \times 1}$ (we assume a single source experiment for sake of compact notation; However, the extension to multiple sources is straightforward). The functions E and F are appropriate regularization functions for \mathbf{m} and $\boldsymbol{\alpha}$, respectively, which are weighted by the penalty parameters μ and $\nu > 0$, respectively. \mathcal{M} and \mathcal{A} are convex sets defined according to our prior knowledge of \mathbf{m} and $\boldsymbol{\alpha}$. For example, if we know the lower and upper bounds on \mathbf{m} and $\boldsymbol{\alpha}$ then

$$\mathcal{M} = \{\mathbf{m} | \mathbf{m}_{min} \leq \mathbf{m} \leq \mathbf{m}_{max}\}, \quad (6)$$

and

$$\mathcal{A} = \{\boldsymbol{\alpha} | \boldsymbol{\alpha}_{min} \leq \boldsymbol{\alpha} \leq \boldsymbol{\alpha}_{max}\}. \quad (7)$$

The PDE constraint $\mathbf{A}(\mathbf{m}, \boldsymbol{\alpha})\mathbf{u} = \mathbf{b}$ in equation 5 is nonlinear in \mathbf{m} and $\boldsymbol{\alpha}$ and very ill-conditioned (Dolean et al., 2015), while the data constraint $\mathbf{P}\mathbf{u} = \mathbf{d}$ is linear but the operator \mathbf{P} is rank-deficient with a huge null space because $M \ll N$. Therefore, determination of the optimum multivariate solution $(\mathbf{u}^*, \mathbf{m}^*, \boldsymbol{\alpha}^*)$ satisfying both constraints (the wave equation and the observation equation) simultaneously is extremely difficult, and requires sophisticated regularizations. In this paper, we use the first-order isotropic TV regularization (Rudin et al., 1992) for

both \mathbf{m} and $\boldsymbol{\alpha}$, i.e. $E(\mathbf{m}) = \|\mathbf{m}\|_{\text{TV}}$ and $F(\boldsymbol{\alpha}) = \|\boldsymbol{\alpha}\|_{\text{TV}}$. However, other regularizations such as compound regularizations can be used in a similar way (see Aghamiry et al., 2019c). The isotropic TV norm of a 2D image $\mathbf{w} \in \mathbb{R}^N$ is defined as (Rudin et al., 1992)

$$\|\mathbf{w}\|_{\text{TV}} = \sum \sqrt{(\nabla_x \mathbf{w})^2 + (\nabla_z \mathbf{w})^2}, \quad (8)$$

where ∇_x and ∇_z are respectively first-order difference operators in the horizontal and vertical directions with appropriate boundary conditions (Gholami and Naeni, 2019).

Beginning with an initial velocity model $\mathbf{v}^0 = 1/\sqrt{\mathbf{m}^0}$ and $\boldsymbol{\alpha}^0 = \mathbf{0}$, $\mathbf{b}^0 = \mathbf{0}$, $\mathbf{d}^0 = \mathbf{0}$, ADMM solves iteratively the multivariate optimization problem, equation 5, with alternating directions as (see Boyd et al., 2010; Benning et al., 2015; Aghamiry et al., 2019e,d, for more details)

$$\begin{cases} \mathbf{u}^{k+1} = \arg \min_{\mathbf{u}} \Psi(\mathbf{u}, \mathbf{m}^k, \boldsymbol{\alpha}^k, \mathbf{b}^k, \mathbf{d}^k) & (9a) \\ \mathbf{m}^{k+1} = \arg \min_{\mathbf{m} \in \mathcal{M}} \Psi(\mathbf{u}^{k+1}, \mathbf{m}, \boldsymbol{\alpha}^k, \mathbf{b}^k, \mathbf{d}^k) & (9b) \\ \boldsymbol{\alpha}^{k+1} = \arg \min_{\boldsymbol{\alpha} \in \mathcal{A}} \Psi(\mathbf{u}^{k+1}, \mathbf{m}^{k+1}, \boldsymbol{\alpha}, \mathbf{b}^k, \mathbf{d}^k) & (9c) \\ \mathbf{b}^{k+1} = \mathbf{b}^k + \mathbf{b} - \mathbf{A}(\mathbf{m}^{k+1}, \boldsymbol{\alpha}^{k+1})\mathbf{u}^{k+1} & (9d) \\ \mathbf{d}^{k+1} = \mathbf{d}^k + \mathbf{d} - \mathbf{P}\mathbf{u}^{k+1}, & (9e) \end{cases}$$

where

$$\begin{aligned} \Psi(\mathbf{u}, \mathbf{m}, \boldsymbol{\alpha}, \mathbf{b}^k, \mathbf{d}^k) &= \mu \|\mathbf{m}\|_{\text{TV}} + \nu \|\boldsymbol{\alpha}\|_{\text{TV}} & (10) \\ &+ \lambda \|\mathbf{b}^k + \mathbf{b} - \mathbf{A}(\mathbf{m}, \boldsymbol{\alpha})\mathbf{u}\|_2^2 + \gamma \|\mathbf{d}^k + \mathbf{d} - \mathbf{P}\mathbf{u}\|_2^2, \end{aligned}$$

is the augmented Lagrangian function written in scaled form (Appendix A), \bullet^k is the value of \bullet at iteration k , the scalars $\lambda, \gamma > 0$ are the penalty parameters assigned to the wave-equation and observation-equation constraints, respectively, and $\mathbf{b}^k, \mathbf{d}^k$ are the scaled Lagrange multipliers, which are updated through a dual ascent scheme by the running sum of the constraint violations (source and data residuals) as shown by equations 9d-9e. The penalty parameters $\lambda, \gamma > 0$ can be tuned in equation 10 such that a dominant weight γ is given to the observation equation at the expense of the wave equation during the early iterations to guarantee the data fit, while the iterative update of the Lagrange multipliers progressively correct the errors introduced by these penalizations such that both of the observation equation and the wave equation are satisfied at the convergence point with acceptable accuracies. In the next three subsections, we show how to solve each optimization subproblem 9a-9c.

Update wavefield (subproblem 9a)

The objective function Ψ is quadratic in \mathbf{u} and its minimization gives the following closed-form expression of \mathbf{u}

$$(\lambda \mathbf{A}^T \mathbf{A} + \gamma \mathbf{P}^T \mathbf{P}) \mathbf{u}^{k+1} = \lambda \mathbf{A}^T (\mathbf{b}^k + \mathbf{b}) + \gamma \mathbf{P}^T (\mathbf{d}^k + \mathbf{d}), \quad (11)$$

where $\mathbf{A} \equiv \mathbf{A}(\mathbf{m}^k, \boldsymbol{\alpha}^k)$ and \mathbf{A}^T denotes the Hermitian transpose of \mathbf{A} .

Update squared slowness (subproblem 9b)

The PDE operator

$$\mathbf{A}(\mathbf{m}, \boldsymbol{\alpha}) = \boldsymbol{\Delta} + \omega^2 \mathbf{C} \text{diag}(\mathbf{m} \circ \rho(\boldsymbol{\alpha})) \mathbf{B} \quad (12)$$

is discretized with the finite-difference method of Chen et al. (2013) where $\boldsymbol{\Delta}$ is the discretized Laplace operator, \mathbf{C} introduces boundary conditions such as perfectly-matched layers (Bérenger, 1994), \mathbf{B} is the mass matrix (Marfurt, 1984) which spreads the mass term $\omega^2 \mathbf{C} \text{diag}(\mathbf{m} \circ \rho(\boldsymbol{\alpha}))$ over all the coefficients of the stencil to improve its accuracy following an anti-lumped mass strategy, and $\text{diag}(\bullet)$ denotes a diagonal matrix. From equation 12 we get that

$$\mathbf{A}(\mathbf{m}, \boldsymbol{\alpha}) \mathbf{u} = \mathbf{A}(\mathbf{0}, \boldsymbol{\alpha}) \mathbf{u} + \omega^2 \mathbf{C} \text{diag}(\mathbf{B} \mathbf{u} \circ \rho(\boldsymbol{\alpha})) \mathbf{m}, \quad (13)$$

where $\mathbf{A}(\mathbf{0}, \boldsymbol{\alpha}) \equiv \boldsymbol{\Delta}$. Therefore, subproblem 9b can be written as

$$\mathbf{m}^{k+1} = \arg \min_{\mathbf{m} \in \mathcal{M}} \mu \|\mathbf{m}\|_{\text{TV}} + \lambda \|\mathbf{L} \mathbf{m} - \mathbf{y}^k\|_2^2, \quad (14)$$

where

$$\mathbf{L} = \omega^2 \mathbf{C} \text{diag}(\mathbf{B} \mathbf{u}^{k+1} \circ \rho(\boldsymbol{\alpha}^k)), \quad (15)$$

and

$$\mathbf{y}^k = \mathbf{b}^k + \mathbf{b} - \boldsymbol{\Delta} \mathbf{u}^{k+1}. \quad (16)$$

Equation 14 describes the box-constrained TV-regularized subproblem for \mathbf{m} which is convex but non-smooth. This box-constrained TV-regularized problem can be solved efficiently with ADMM and splitting methods, also referred to as the split Bregman method (Goldstein and Osher, 2009). Using splitting methods, the unconstrained subproblem 14 is recast as a multivariate constrained problem, through the introduction of auxiliary variables. These auxiliary variables are introduced to decouple the ℓ_2 subproblem from the ℓ_1 subproblem such that they can be solved in alternating mode with ADMM. Moreover, a closed form expression of the auxiliary variables is easily obtained by solving the ℓ_1 subproblem with proximity operators (Combettes and Pesquet, 2011; Parikh and Boyd, 2013). We refer the reader to Appendix B for a more detailed review of this method.

Update attenuation factor (subproblem 9c)

Subproblem 9c is nonlinear due to the nonlinearity of the PDE with respect to $\boldsymbol{\alpha}$. We linearize this subproblem by using a first-order approximation of $\rho(\alpha)$, equation 4, as

$$\rho(\alpha) \approx 1 + 2\beta(\omega)\alpha, \quad (17)$$

which is accurate for $\alpha \ll 1$ (Hak and Mulder, 2011), and gives

$$\mathbf{A}(\mathbf{m}, \boldsymbol{\alpha}) \mathbf{u} \approx \mathbf{A}(\mathbf{m}, \mathbf{0}) \mathbf{u} + 2\omega^2 \beta(\omega) \mathbf{C} \text{diag}(\mathbf{B} \mathbf{u} \circ \mathbf{m}) \boldsymbol{\alpha}. \quad (18)$$

Accordingly, subproblem 9c can be written as the following linear problem

$$\boldsymbol{\alpha}^{k+1} \approx \arg \min_{\boldsymbol{\alpha} \in \mathcal{A}} \nu \|\boldsymbol{\alpha}\|_{\text{TV}} + \lambda \|\mathbf{H} \boldsymbol{\alpha} - \mathbf{h}^k\|_2^2, \quad (19)$$

where

$$\mathbf{H} = 2\omega^2 \beta(\omega) \mathbf{C} \text{diag}(\mathbf{B} \mathbf{u}^{k+1} \circ \mathbf{m}^{k+1}), \quad (20)$$

and

$$\mathbf{h}^k = \mathbf{b}^k + \mathbf{b} - \mathbf{A}(\mathbf{m}^{k+1}, \mathbf{0}) \mathbf{u}^{k+1}. \quad (21)$$

Equation 19 is also a box-constrained TV-regularized convex problem, which can be solved with ADMM (Appendix A) in a manner similar to the previous subproblem for squared slowness. It is important to stress that the errors generated by the first-order approximation of $\rho(\boldsymbol{\alpha})$ during the update of $\boldsymbol{\alpha}$ are iteratively compensated by the action of the scaled Lagrange multiplier \mathbf{b}^k . These Lagrange multipliers are formed by the running sum of the wave equation errors, which are computed with the exact wave equation operator (namely, without linearization of $\rho(\boldsymbol{\alpha})$).

The overall workflow described above is summarized in Algorithm 1.

Practical implementation

The ADMM optimization that is used to solve equations 14 and 19 is reviewed in Appendix B. We also refer the reader to Goldstein and Osher (2009), Boyd et al. (2010) and Aghamiry et al. (2019d) as a complement. A key property of the ADMM algorithm, equation 9, is that, at iteration k , we don't need to solve each optimization subproblems 9a-9c exactly via inner iterations. The intuitive reason is that the updating of the primal variable performed by one subproblem is hampered by the errors of the other primal variables that are kept fixed. In this framework, the errors at each iteration k are more efficiently compensated by the gradient-ascent update of the Lagrange multipliers (dual variable). This statement was corroborated by numerical experiments which showed that one (inner) iteration of each subproblem per ADMM cycle k generates solutions which are accurate enough to guarantee the fastest convergence of the ADMM algorithm (Goldstein and Osher, 2009; Boyd et al., 2010; Aghamiry et al., 2019d; Gholami et al., 2018; Aghamiry et al., 2019b). Moreover, this error compensation is more efficient when the dual variables are updated after each primal subproblem 9a-9c rather than at the end of an iteration k as indicated in Algorithm 1 for sake of compactness. This variant of ADMM is referred to as the Peaceman-Rachford splitting method (Peaceman and Rachford, 1955; He et al., 2014) and will be used in the following numerical experiments. The reader is referred to Aghamiry et al. (2019e) for more details about the improved convergence of the Peaceman-Rachford splitting method compared to ADMM in the framework of IR-WRI.

We follow the guideline presented in Aghamiry et al. (2019d, section 3.1) for tuning the penalty parameters. The overall procedure is as follow: we first set $\mu=0.6$ and $\nu=0.4$ to tune the relative weight of the regularizations of the squared slowness (\mathbf{m}) and attenuation factor ($\boldsymbol{\alpha}$), equation 10. Then, we set the ratios μ/ξ_m and ν/ξ_α ,

lines 7, 9, 10, 12 in Algorithm 1, to tune the soft thresholding performed by the TV regularization of \mathbf{m} and α (subproblems 9b and 9c). We refer the reader to Appendix B for the role of the penalty parameters ξ_m and ξ_α in TV regularization (denoted generically by ξ in equation B-3). We set μ/ξ_m and ν/ξ_α equal to $0.02 \times \max(\mathbf{r})$, equations B-19. These values can be refined according to our prior knowledge of the subsurface medium. Then, we set a constant λ to balance the relative weight of the regularization and the wave-equation misfit function during the parameter-estimation subproblems, equations 14 and 19, and lines 5 and 6 in Algorithm 1. If necessary, λ can be increased during iterations to mitigate the imprint of the regularization near the convergence point. Finally, we set γ for wavefield reconstruction such that λ/γ is a small fraction of the highest eigenvalue of the regularized normal operator, equation 11 and line 1 in Algorithm 1 (van Leeuwen and Herrmann, 2016). This parameter γ can be kept constant during iterations. The reader is referred to Aghamiry et al. (2019e) for an analysis of the sensitivity of IR-WRI to the choice of the weight balancing the role of the observation equation and the wave equation during wavefield reconstruction.

NUMERICAL EXAMPLES

Simple inclusions test

We first consider a simple 2D example to validate viscoacoustic IR-WRI without and with TV regularization. The true velocity model is a homogeneous background model with a wavespeed of 1.5 km/s, which contains two inclusions: a 250-m-diameter circular inclusion at position (1 km, 1.6 km) with a wavespeed of 1.8 km/s and a 0.2×0.8 km rectangular inclusion at the center of the model with a wavespeed of 1.3 km/s (Figure 1a). Also, the true α model is a homogeneous background model with $\alpha=0.01$ ($\mathbf{Q} = 100$), which contains two inclusions, both of them with $\alpha = 0.1$ ($\mathbf{Q} = 10$). The first is a 250-m-diameter circular inclusion at position (1 km, 0.4 km) and the second is a 0.2×0.8 km rectangle inclusion at the center of the model (Figure 1b). The wavespeed and α rectangular inclusions share the same size and position, while the position of the wavespeed and α circular inclusions are different in order to test different parameter trade-off scenarios. A vertical and horizontal logs which cross the center of \mathbf{v} and α models are plotted in the left and bottom side of the models, respectively, for all the figures of this test. An ideal acquisition is used with 8 sources and 200 receivers along the four edges of the model and three frequency components (2.5, 5, 7 Hz) are jointly inverted using a maximum of 30 iterations as stopping criterion of iteration.

We performed viscoacoustic IR-WRI without and with TV regularization starting from homogeneous \mathbf{v} and α models with $\mathbf{v} = 1.5$ km/s and $\alpha = 0$, respectively. The final (\mathbf{v}, α) models estimated by IR-WRI without and with TV regularization are shown in Figures 1c-d and

1e-f, respectively. The IR-WRI results without TV regularization show acceptable velocity model and quite noisy attenuation reconstruction (Figure 1c-d). The velocity reconstruction is however hampered by significant limited bandwidth effects. We also show underestimated wavespeeds in the rectangular inclusion along the horizontal log. These underestimated wavespeeds are clearly correlated with underestimated α values (overestimated \mathbf{Q}), hence highlighting some trade-off between \mathbf{v} and α . Other moderate trade-off artifacts are shown in the vertical log of the α model, which shows undesired high-frequency perturbations at the position of the circular velocity inclusion. The TV regularization removes very efficiently all of these pathologies: it extends the wavenumber bandwidth of the models and removes to a large extent the parameter cross-talk as the subsurface medium perfectly matches the piecewise-constant prior associated with TV regularization (Figure 1e-f). Note however that α remains slightly underestimated in the circular inclusion (Figure 1f). This correlates with a barely-visible velocity underestimation at this location in Figure 1e. The relative magnitude of these errors gives some insight on the relative sensitivity of the data to \mathbf{m} and α .

Synthetic North Sea case study

Experimental setup

We consider a more realistic 16 km \times 5.2 km shallow-water synthetic model representative of the North Sea (Munns, 1985). The true \mathbf{v} and α models are shown in Figures 2a and 2b, respectively. The velocity model is formed by soft sediments in the upper part, a pile of low-velocity gas layers above a chalk reservoir, the top of which is indicated by a sharp positive velocity contrast at around 2.5 km depth, and a flat reflector at 5 km depth (Figure 2a). The α model has two highly attenuative zones in the upper soft sediments and gas layers, and the α value is relatively low elsewhere (Figure 2b).

The fixed-spread surface acquisition consists of 320 explosive sources spaced 50 m apart at 25 m depth and 80 hydrophone receivers spaced 200 m apart on the sea floor at 75 m depth. For sake of computational efficiency, we use the spatial reciprocity of Green's functions to process sources as receivers and vice versa. A free-surface boundary condition is used on top of the grid and the source signature is a Ricker wavelet with a 10 Hz dominant frequency. We perform forward modeling with a nine-point stencil finite-difference method implemented with anti-lumped mass and PML absorbing boundary conditions, where the stencil coefficients are optimized to the frequency (Chen et al., 2013). We solve the normal-equation system for wavefield reconstruction, equation 11, with a sparse direct solver (Duff et al., 1986). The initial model for \mathbf{v} is a highly Gaussian filtered version of the true model (Figure 2c), while the starting α model is homogeneous with $\alpha = 0$. The common-shot gathers computed in the true and initial models are compared in Figure 3 for a

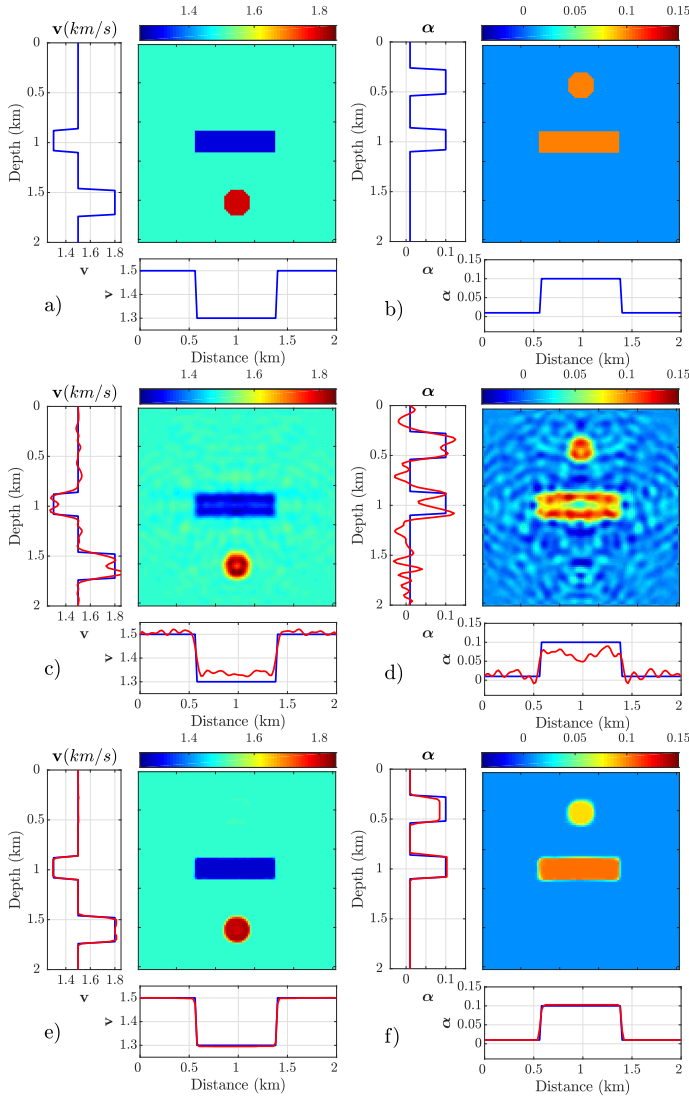


Figure 1: (a) True velocity model. (b) True attenuation model. (c-d) Reconstructed velocity (c) and attenuation (d) from viscoacoustic IR-WRI without TV regularization. (e-f) Same as (a-b) when TV regularization is applied. Profiles of the true (blue) and reconstructed (red) models running across the center of the models are shown on the left and bottom of the reconstructed models.

shot located at 16.0 km. The latter mainly show the direct wave and the diving waves, which are highly cycle skipped relative to those computed in the true model.

We perform the inversion with small batches of three frequencies with one frequency overlap between two consecutive batches, moving from the low frequencies to the higher ones according to a classical frequency continuation strategy. The starting and final frequencies are 3 Hz and 15 Hz and the sampling interval in each batch is 0.5 Hz. We perform three paths through the frequency batches to improve the results, using the final model of one path as the initial model of the next one (these paths can be viewed as outer iterations of the algorithm). The start-

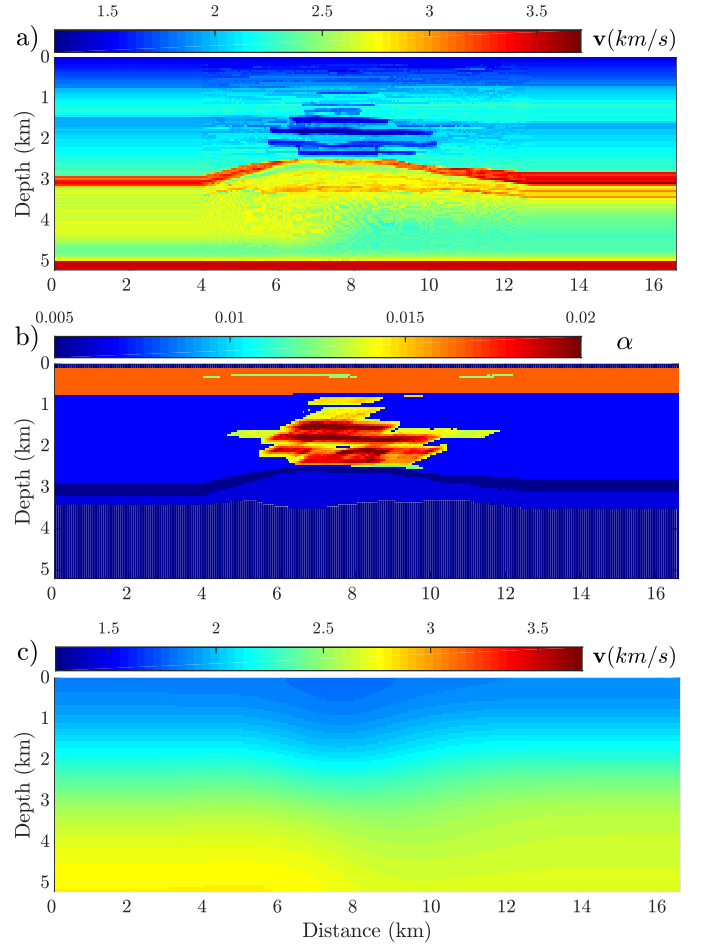


Figure 2: North Sea case study. (a) True v model. (b) True α model. (c) Initial v model.

ing and finishing frequencies of the paths are [3, 6], [4, 10], [6, 15] Hz respectively, where the first and second elements of each pair show the starting and finishing frequencies, respectively. Also, we used batches of four frequencies with two frequencies overlap during the second path and five frequencies with three frequencies overlap during the third path. The motivation behind this frequency management is to keep the bandwidth of each patch narrow during the first path in order to mitigate nonlinearities through a progressive frequency continuation, before broadening this bandwidth during the second and third paths to strengthen the imprint of dispersion in the inversion and decouple velocity and attenuation more efficiently.

Comparison of FWI and WRI objective Functions

Before showing the inversion results, it is worth illustrating how WRI extends the search space of FWI for this North Sea case study. For this purpose, we compare the shape of the classical FWI misfit function based upon the ℓ_2 norm of the data residuals (e.g. Pratt et al., 1998) with that of the parameter-estimation WRI subproblem for the 3 Hz frequency and for a series of v and α models

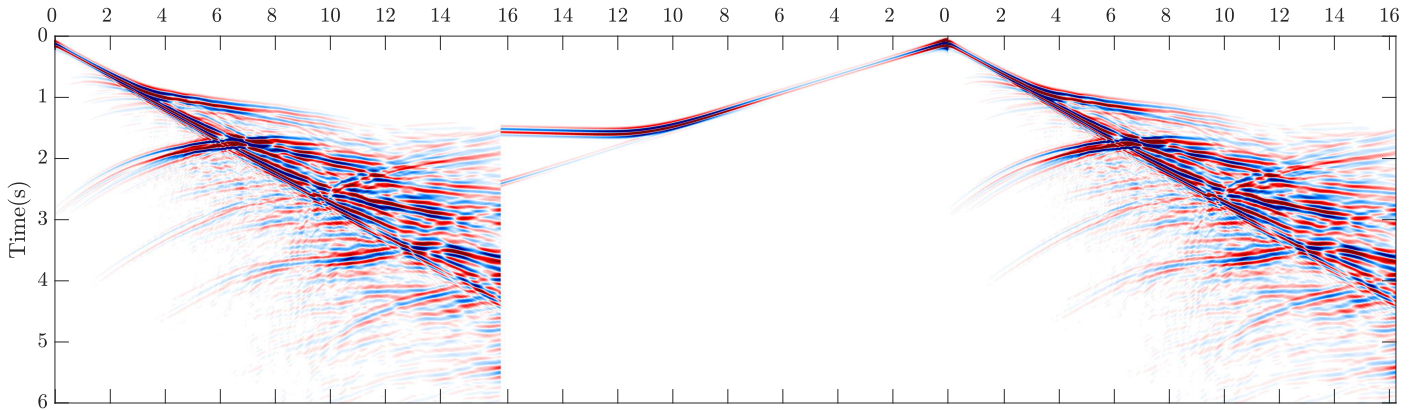


Figure 3: Time domain seismograms computed in the true and initial models. The true seismograms are shown in the left and right panels, while those computed in the initial model are shown in the middle panel with a mirror representation such that the two sets of seismograms can be compared at long and short offsets. The seismograms are plotted with a reduction velocity of 2.5 km/s for sake of time axis compression.

that are generated according to

$$\mathbf{v}_a = \mathbf{v}_{true} + a^2(\mathbf{v}_{init} - \mathbf{v}_{true}), \quad (22a)$$

$$\boldsymbol{\alpha}_b = \boldsymbol{\alpha}_{true} + b^2(\boldsymbol{\alpha}_{init} - \boldsymbol{\alpha}_{true}), \quad (22b)$$

where $-1 \leq a, b \leq 1$. In this case, $(\mathbf{v}_a, \boldsymbol{\alpha}_b)$ lies on the line-segment joining the initial point $(\mathbf{v}_{init}, \boldsymbol{\alpha}_{init})$ and final point $(\mathbf{v}_{true}, \boldsymbol{\alpha}_{true})$. We set \mathbf{v}_{true} and $\boldsymbol{\alpha}_{true}$ as those shown in Figures 2(a-b), \mathbf{v}_{init} as the initial \mathbf{v} model shown in Figure 2c, and $\boldsymbol{\alpha}_{init}$ as a homogeneous model with $\boldsymbol{\alpha} = 0.004$ ($\mathbf{Q} = 250$). The misfit functions of FWI and WRI are shown in Figures 4a and 4b, respectively. The FWI objective function exhibits spurious local minima with respect to both velocity and attenuation (a and b dimensions), while only one minimum is seen in the WRI objective function. Indeed, this highlights the search space expansion generated by the wave-equation relaxation during WRI. This search space expansion is displayed through a wider and flatter attraction basin compared to that of FWI. This wide attraction basin exacerbates the contrast between the sensitivities of the objective function to velocity and attenuation, with a quite weak sensitivity to the latter. These contrasted sensitivities would likely make the parameter estimation subproblem poorly scaled if the velocity and attenuation were jointly updated during WRI based on variable projection (van Leeuwen and Herrmann, 2016). In this context, the alternating-direction strategy can be viewed as an heuristic to overcome this scaling issue. Indeed, the lack of sensitivity to attenuation during the early WRI iterations requires aggressive regularization and bound constraints to stabilize the attenuation estimation. As WRI proceeds over iterations and the wave equation constraint is satisfied more accurately, the inversion should recover a significant sensitivity to attenuation as that highlighted in Figure 4a allowing for a relaxation of the regularization. These statements highlight the need to reconcile search space expansion to manage nonlinearity and regularization plus bound constraints to restrict the

range of feasible solutions for $\boldsymbol{\alpha}$.

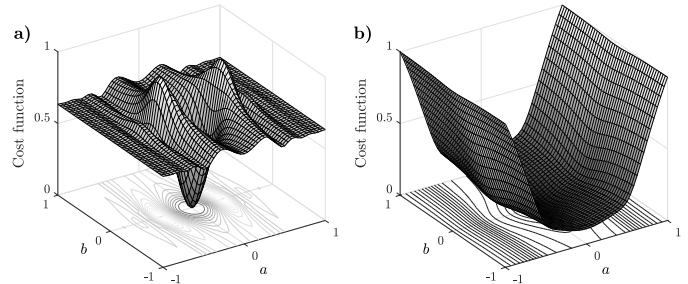


Figure 4: The objective function for the 3 Hz wavefield as a function of \mathbf{v}_a and $\boldsymbol{\alpha}_b$ generated using equation 22. (a) Classical reduced-space FWI. (b) WRI.

Viscoacoustic FWI results

To show the need of search space expansion and regularization, we first perform a classical viscoacoustic FWI for noiseless data (e.g. Kamei and Pratt, 2013; Operto and Miniussi, 2018). We use squared-slowness and attenuation as optimization parameters and update them simultaneously with the L-BFGS quasi-Newton optimization and a line search procedure for step length estimation (that satisfies the Wolfe conditions). Neither TV regularization nor bound constraints are applied. Owing the limited kinematic accuracy of the initial models highlighted by the seismograms mismatches in Figure 3, the reconstruction of the velocity model remains stuck in a local minimum during the first frequency batch inversion (Figure 5a), while the estimated attenuation model shows unrealistic values due to the lack of bound constraints (Figure 5b). This failure prompts us to stop the inversion at this stage.

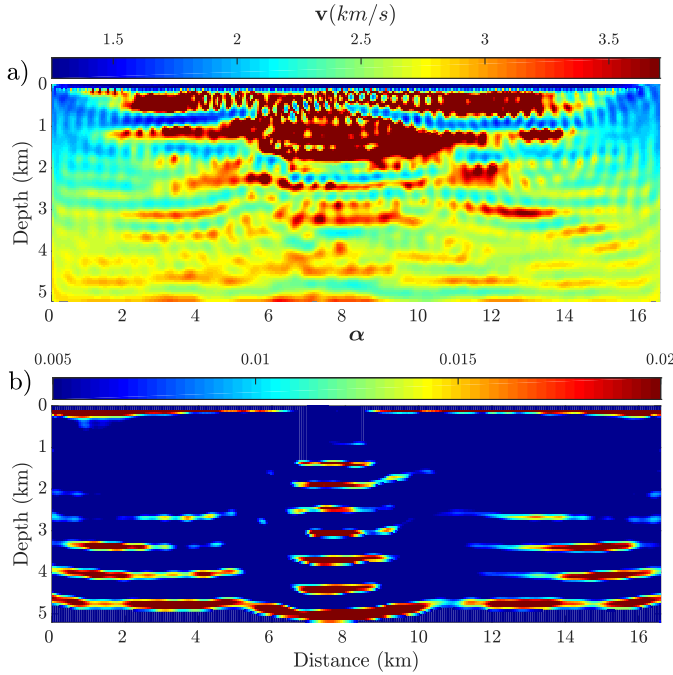


Figure 5: Viscoacoustic FWI results after inverting the first frequency batch. (a) Reconstructed velocity model. (b) Reconstructed attenuation model. TV regularization and bound constraints are not applied.

Viscoacoustic IR-WRI results

We now update \mathbf{v} and α with IR-WRI according to the optimization workflow described in Algorithm 1. IR-WRI is performed without and with bound constraints + TV regularization (referred to as BTV regularization in the following). The lower and upper bounds are 1.2 km/s and 4 km/s for velocities, and 0.001 and 0.025 for α . For each case, the stopping criterion for each batch is given to be either reaching a maximum iteration count of 20 or

$$\begin{aligned} \sum \|\mathbf{A}(\mathbf{m}^{k+1}, \alpha^{k+1})\mathbf{u}^{k+1} - \mathbf{b}\|_2^2 &\leq \epsilon_b \quad \text{and} \\ \sum \|\mathbf{P}\mathbf{u}^{k+1} - \mathbf{d}\|_2^2 &\leq \epsilon_d, \end{aligned} \quad (23)$$

where the sums run over the frequencies of the current batch, $\epsilon_b=1e-3$ and $\epsilon_d=1e-5$. We start with inversion of noiseless data. The final \mathbf{v} and α models, estimated by IR-WRI without and with BTV regularization, are shown in Figure 6(a-d) after 360 and 321 iterations, respectively. A direct comparisons between the logs extracted from the true models, the initial model and the IR-WRI velocity models reconstructed without/with BTV regularization at $x = 3.5$ km, $x = 8.0$ km and $x = 12.0$ km are shown in Figure 7a. Although a crude initial velocity model was used, the velocities in the shallow sedimentary cover and the gas layers are fairly well reconstructed in both cases (Figure 6a,c). Also, IR-WRI without BTV regularization manages to reconstruct an acceptable velocity model unlike classical FWI (Figure 5). The main differences between the IR-WRI velocity models built with and without

BTV regularization are shown at the reservoir level and below. Without BTV regularization, the top of the reservoir is mispositioned (Figure 7a, $x = 8.0$ km, green versus red curves) and the inversion fails to reconstruct the smoothly-decreasing velocity below it due to the lack of diving wave illumination at these depths (Figure 7a). This in turn prevents the focusing of the deep reflector at 5 km depth by migration of the associated short-spread reflections (Figure 6a). When BTV regularization is used, viscoacoustic IR-WRI provides a more accurate and cleaner images of the reservoir and better reconstructs the sharp contrast on top of it (Figure 6c). As expected, the TV regularization replaces the smoothly-varying velocities below the reservoir (between 3 to 5 km depth) by a piecewise-constant layer due to the lack of wave illumination in this part of the model (Figure 7a, green curves). However, this does not prevent a fairly accurate reconstruction of the deep reflector at 5 km depth.

A direct comparisons between the logs extracted from the true and the IR-WRI attenuation models at $x = 3.5$ km, $x = 8.0$ km and $x = 12.0$ km are shown in Figure 7b. The reconstruction of α without BTV regularization is quite unstable, with an oscillating trend and overestimated values (Figures 6b and red curves in 7b). This highlights fairly well the ill-posedness of the attenuation reconstruction. In contrast, the α model reconstructed with BTV regularization captures the large-scale attenuation trend in the shallow sedimentary cover, in the gas layers and below the reservoir (Figures 6d and green curves in 7b). We note however that the attenuation is underestimated on top of the gas layers between 1 km and 1.4 km depth (Figure 7b, $x = 8.0$ km, green curve). This error in the attenuation reconstruction might be correlated with subtle underestimation of velocities at these depths (Figure 7a, $x = 8$ km, green curve). This might indicate on the one hand some mild amplitude-related cross-talk effects between velocities and attenuation and on the other hand the higher sensitivity of the data to velocities compared to attenuation (in the sense that a small error in the velocity contrasts can compensate more significant attenuation errors). Similar cross-talk artifacts have been previously discussed during the toy inclusion test (Figure 1e-f).

We continue by assessing the resilience of the proposed viscoacoustic IR-WRI to noise when data are contaminated with a Gaussian random noise with a SNR=10 db. Here, SNR is defined based on the root mean square (RMS) amplitude of signal and that of noise as

$$\text{SNR} = 20 \log \left(\frac{\text{Signal RMS Amplitude}}{\text{Noise RMS Amplitude}} \right). \quad (24)$$

We use the same setup and the same initial models as those used for the noiseless case. The stopping criterion is defined by equation 23, where ϵ_d is now set to the noise level. The final models of IR-WRI obtained without and with BTV regularization are shown in Figure 6(e-h). The total number of IR-WRI iterations are 196 and 185, respectively, for these results. In a similar manner to the

noiseless case, a direct comparisons between the logs extracted from the true models, the initial model and the IR-WRI velocity models at $x = 3.5$ km, $x = 8.0$ km and $x = 12.0$ km are shown in Figure 8. Overall, a similar trend as for the noiseless case is shown. However, the presence of noise in the data leads to a mispositioning of the reservoir at 8 km distance in the BTV IR-WRI velocity model, which was not observed in the noiseless case (compare Figures 7a and 8a, $x = 8$ km, green curves). This mispositioning of the reservoir may be correlated with a poorer reconstruction of the attenuating gas layers between 1 km and 2.5 km depth (compare Figures 7b and 8b, $x = 8$ km, green curves).

We also compute a common-shot gather for a shot located at 16.0 km in the IR-WRI models inferred from noiseless/noisy data with/without BTV regularization (Figure 9). The time-domain seismograms computed in the IR-WRI models obtained without regularization (Figure 9a and 9c) show underestimated amplitudes and do not match late dispersive arrivals due to the overestimated and oscillating values of α (Figures 6b and 7b for noiseless data and Figures 6f and 8b for noisy data).

In the case of noiseless data, the bound constraints and the TV regularization allow for a high-quality data fit (Figure 9c), consistently with the accuracy of the models shown in Figure 6c-d. In the case of noisy data, the bound constraints and the TV regularization improve significantly the data match (compare Figure 9c and Figure 9d). However, the imprint of the cross-talk artifacts mentioned above are clearly seen at long offsets with a degraded fit of deeply-propagating waves (for example, the refracted wave from the deep reflector at around 1.5s traveltime and the late dispersive waves at around 4 s traveltime) relative to the noiseless-data results (compare Figure 9b and Figure 9d).

CONCLUSIONS

We extended the recently proposed ADMM-based iteratively-refined wavefield reconstruction inversion (IR-WRI) for attenuation imaging by inversion of viscoacoustic wavefields. The proposed viscoacoustic IR-WRI treats the nonlinear viscoacoustic waveform inversion as a multiconvex optimization problem. To achieve this goal, the original nonlinear multi-parameter problem for squared slowness and attenuation factor is replaced by three recursive linear mono-parameter subproblems for wavefield, squared slowness and attenuation factor that are solved in alternating mode at each IR-WRI iteration. The attenuation-reconstruction subproblem requires to introduce an approximate multilinear viscoacoustic wave equation in wavefield, squared slowness, and attenuation factor. However, the errors generated by this approximate viscoacoustic wave equation during the attenuation reconstruction are efficiently compensated by the Lagrange multipliers (namely, the running sum of the wave equation errors) that are computed with the exact viscoacoustic equation. This new formulation has first the flexibility to tailor the

regularization to the squared slowness and attenuation factor. Moreover, it simplifies the multi-parameter optimization workflow and mitigates its computational cost since the original poorly-scaled multi-parameter inversion is recast as two interlaced mono-parameter inversions. A realistic synthetic example suggests that the search space extension embedded in IR-WRI efficiently mitigates cycle skipping when a crude initial velocity model is used, while the TV-regularized alternating-direction optimization reasonably manages the cross-talks between squared slowness and attenuation as well as the limited sensitivity of the data to the attenuation.

APPENDIX A

SCALED FORM OF AUGMENTED LAGRANGIAN

In this appendix, we briefly review how augmented Lagrangian (AL) function, as the one shown in equation 10, is used to solve constrained problem with the method of multiplier (Nocedal and Wright, 2006b, Chapter 17). Let's start with the following constrained problem

$$\min_{\mathbf{x}} \|P(\mathbf{x})\|_2^2 \quad \text{subject to} \quad Q(\mathbf{x}) = \mathbf{0}. \quad (\text{A-1})$$

The AL function associated with the problem A-1 combines a Lagrangian function and a penalty function as

$$\mathcal{L}_A(\mathbf{x}, \mathbf{v}) = \underbrace{\|P(\mathbf{x})\|_2^2 + \langle \mathbf{v}, Q(\mathbf{x}) \rangle}_{\text{Lagrangian}} + \underbrace{\frac{\xi}{2} \|Q(\mathbf{x})\|_2^2}_{\text{Augmentation}}, \quad (\text{A-2})$$

where $\langle \cdot, \cdot \rangle$ denotes inner product and \mathbf{v} and ξ denotes the Lagrange multiplier (dual variable) and the penalty parameter, respectively.

This AL function can be written in a compact form by introducing the scaled dual variable $\mathbf{q} = -\mathbf{v}/\xi$ and adding and subtracting the term $\frac{\xi}{2} \|\mathbf{q}\|_2^2$ to the function A-2 (See Boyd et al., 2010, Page 15 for more details):

$$\begin{aligned} \mathcal{L}_A(\mathbf{x}, \mathbf{q}) &= \|P(\mathbf{x})\|_2^2 - \xi \langle \mathbf{q}, Q(\mathbf{x}) \rangle + \frac{\xi}{2} \|Q(\mathbf{x})\|_2^2 + \frac{\xi}{2} \|\mathbf{q}\|_2^2 - \frac{\xi}{2} \|\mathbf{q}\|_2^2 \\ &= \|P(\mathbf{x})\|_2^2 + \frac{\xi}{2} \|Q(\mathbf{x}) - \mathbf{q}\|_2^2 - \frac{\xi}{2} \|\mathbf{q}\|_2^2. \end{aligned} \quad (\text{A-3})$$

Equation A-3 shows the augmented Lagrangian method can be seen as a penalty method with an error correction term in the penalty function, $\frac{\xi}{2} \|Q(\mathbf{x}) - \mathbf{q}\|_2^2$, corresponding to the scaled Lagrange multipliers. This correction term controls how well the constraint is satisfied at the convergence point. In the framework of the method of multiplier, the AL function is minimized with respect to the primal variable \mathbf{x} and maximized with respect to the scaled dual variable \mathbf{q} in alternating mode. Expression A-3 shows that the dual variable is simply updated with the constraint violation when a gradient ascent method is used. This recipe has been used to derive equation 9 with ADMM (AL method with alternating update of multiple classes of primal variable). The reader is referred to Aghamiry et al. (2019e) for the detailed development.

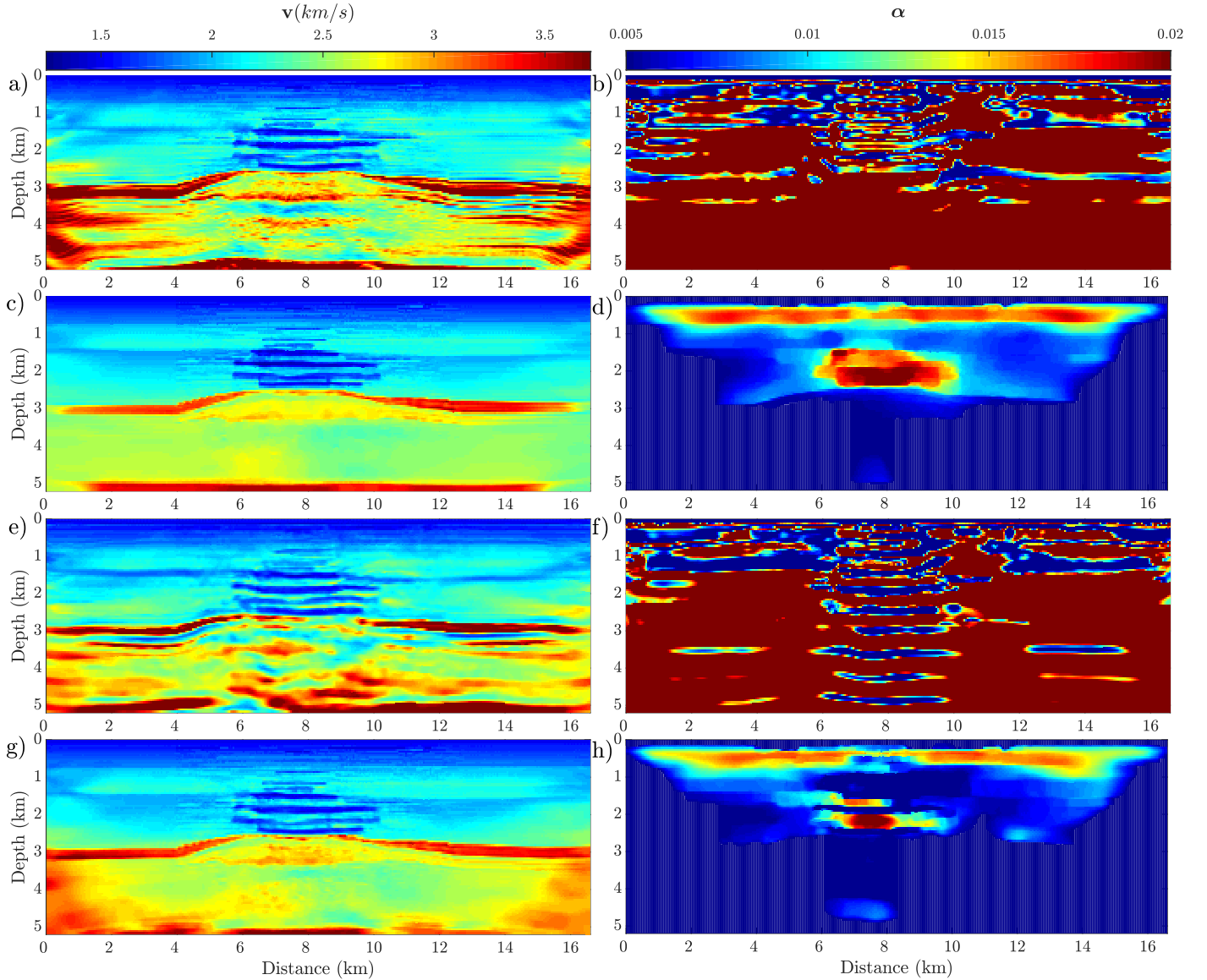


Figure 6: Viscoacoustic IR-WRI results. (a-d) Noiseless data. (a-b) Velocity (a) and attenuation (b) models reconstructed without BTV regularization. (c-d) Same as (a-b) when BTV regularization is applied. (e-h) Same as (a-d) for noisy data (SNR=10db).

APPENDIX B

BOUND CONSTRAINED TV-REGULARIZATION USING ADMM

In this appendix, we review step by step how to solve a bound-constrained TV-regularized convex problem (such as those in equations 14 and 19) using variable splitting and ADMM (Boyd et al., 2010). Let’s consider a general bound-constrained TV-regularized convex problem of the form

$$\min_{\mathbf{x} \in \mathcal{X}} \sum_{i=1}^N \sqrt{|\nabla_x \mathbf{x}|_i^2 + |\nabla_z \mathbf{x}|_i^2} + \frac{\lambda}{2} \|\mathbf{G}\mathbf{x} - \mathbf{y}\|_2^2, \quad (\text{B-1})$$

for some column vector \mathbf{y} and matrix \mathbf{G} . The model \mathbf{x} is an N -length column vector, ∇_x and ∇_z are square first-

order difference matrices, and \mathcal{X} is the desired convex set. The penalty parameter $\lambda > 0$ balances the relative weight of the TV regularizer and the misfit term. Following Aghamiry et al. (2019d, section 2.2.2), equation B-1 can be solved via the following three easy tricks.

1) *Variable splitting*. Since the variable \mathbf{x} appears simultaneously in the TV, misfit, and bounding terms, it “couples” these terms and makes it difficult to solve the problem. To decouple them, new auxiliary variables $\mathbf{p}_x = \nabla_x \mathbf{x}$, $\mathbf{p}_y \in \mathcal{X}$, and $\mathbf{p}_z = \nabla_z \mathbf{x}$ are substituted in the TV term and the bound constraint, respectively, and their expression as a function of the original variable \mathbf{x} are introduced as new equality constraints. This recasts B-1 as the fol-

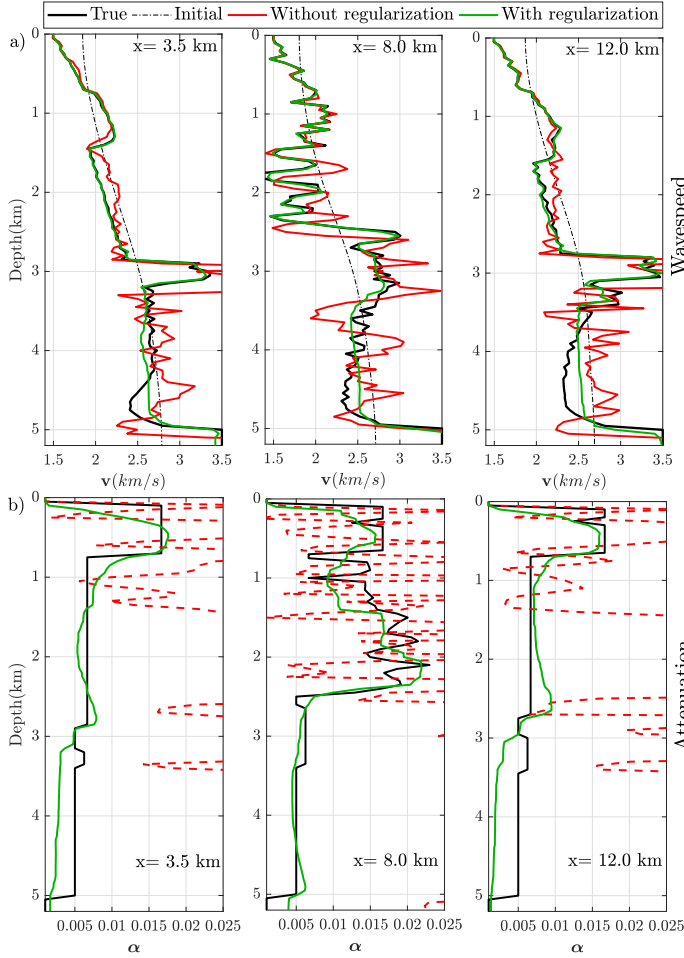


Figure 7: For noiseless data, direct comparison along the logs at $x = 3.5$ (left), $x = 8.0$ (center) and $x = 12.0$ km (right) between the true model (black), the initial model (dashed line) and the IR-WRI models without (red) and with BTV (green) regularization (Figure 6(a-d)). (a) Estimated \mathbf{v} , (b) estimated α .

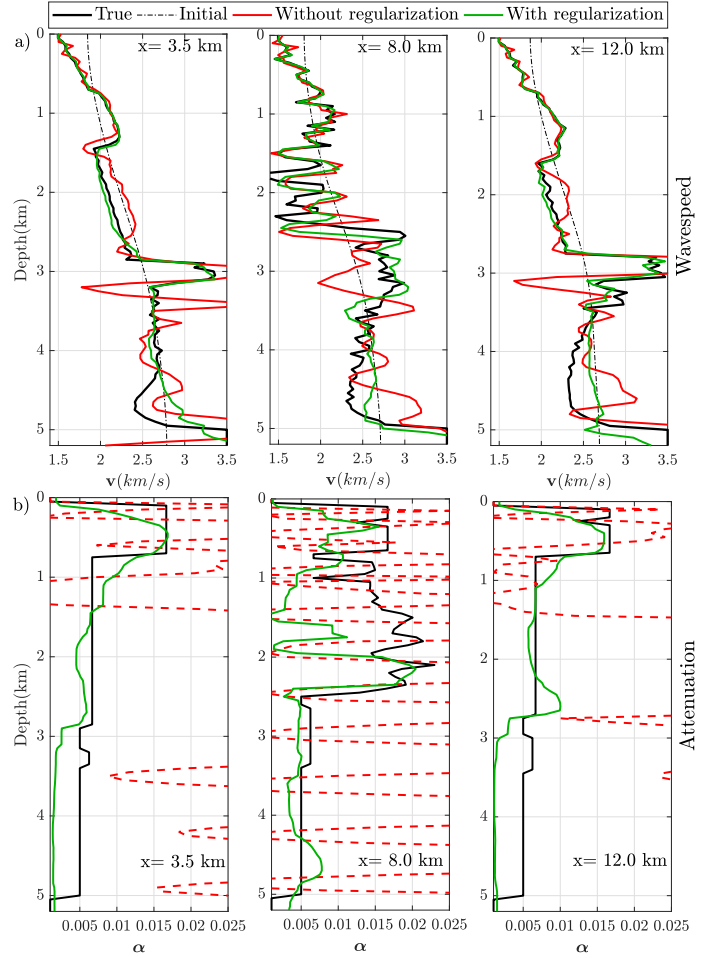


Figure 8: Same as Fig. 7 but for noisy data with SNR=10db. The corresponding IR-WRI models are shown in Figure 6(e-h)).

lowing constrained problem

$$\min_{\mathbf{x}, \mathbf{p}_x, \mathbf{p}_y \in \mathcal{X}, \mathbf{p}_z} \sum_{i=1}^N \sqrt{|\mathbf{p}_x|_i^2 + |\mathbf{p}_z|_i^2} + \frac{\lambda}{2} \|\mathbf{G}\mathbf{x} - \mathbf{y}\|_2^2 \quad (\text{B-2})$$

$$\text{subject to } \begin{cases} \mathbf{p}_x = \nabla_x \mathbf{x}, \\ \mathbf{p}_y = \mathbf{x}, \\ \mathbf{p}_z = \nabla_z \mathbf{x}. \end{cases}$$

2) *Augmented Lagrangian*. The second trick is to relax these new linking constraints with an augmented Lagrangian function. This recasts B-2 as the following min-

max optimization problem

$$\begin{aligned} \min_{\mathbf{x}, \mathbf{p}_x, \mathbf{p}_y \in \mathcal{X}, \mathbf{p}_z} \max_{\mathbf{q}_x, \mathbf{q}_y, \mathbf{q}_z} & \sum_{i=1}^N \sqrt{|\mathbf{p}_x|_i^2 + |\mathbf{p}_z|_i^2} + \frac{\lambda}{2} \|\mathbf{G}\mathbf{x} - \mathbf{y}\|_2^2 \\ & + \langle \mathbf{q}_x, \mathbf{p}_x - \nabla_x \mathbf{x} \rangle + \frac{\xi}{2} \|\mathbf{p}_x - \nabla_x \mathbf{x}\|_2^2 \\ & + \langle \mathbf{q}_y, \mathbf{p}_y - \mathbf{x} \rangle + \frac{\xi}{2} \|\mathbf{p}_y - \mathbf{x}\|_2^2 \\ & + \langle \mathbf{q}_z, \mathbf{p}_z - \nabla_z \mathbf{x} \rangle + \frac{\xi}{2} \|\mathbf{p}_z - \nabla_z \mathbf{x}\|_2^2, \quad (\text{B-3}) \end{aligned}$$

where $\mathbf{q}_x, \mathbf{q}_y, \mathbf{q}_z$ are Lagrange multipliers (dual variables), and $\xi > 0$ is the penalty parameter. Note that, here we used the same penalty parameter for all three constraints but one may use different parameter for each of them. The augmented Lagrangian method (a.k.a. method of multipliers, Hestenes, 1969) maximizes the objective in equation B-3 with respect to the dual variables iteratively by using a simple steepest ascent algorithm (with step length

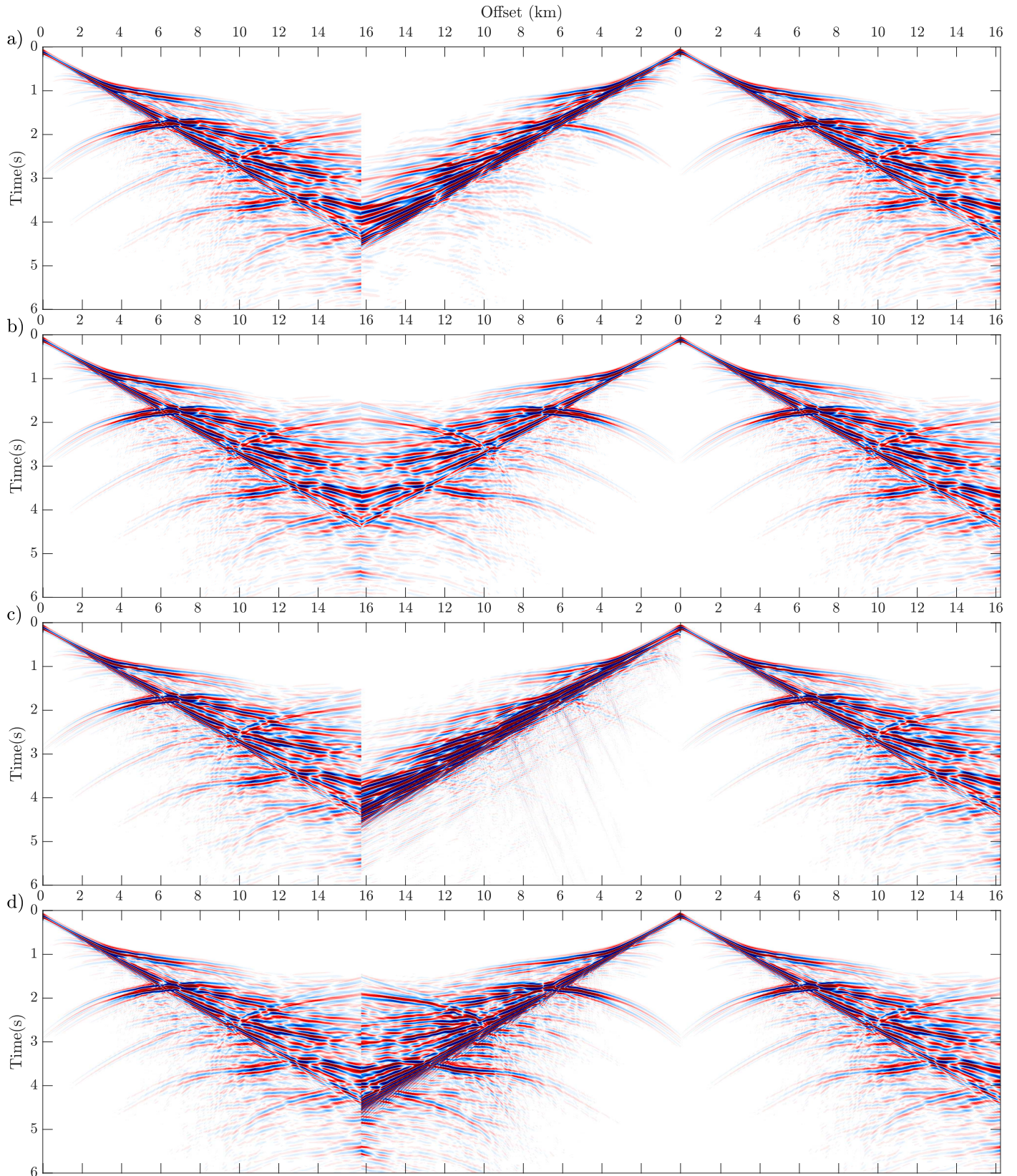


Figure 9: Time domain seismograms computed in (a) IR-WRI without regularization and (b) BTV regularized IR-WRI for noiseless data (Figure 6a- 6d). (c-d) Same as (a-b), but for noisy data (Figure 6e- 6h). The true seismograms are shown in the first and the last panel of the above mentioned seismograms (folded) to have a comparison at short and long offset with true seismograms. The seismograms are plotted with a reduction velocity of 2.5 km/s for sake of time axis compression.

ξ)

$$\mathbf{q}_x^{k+1} = \mathbf{q}_x^k + \xi(\mathbf{p}_x^{k+1} - \nabla_x \mathbf{x}^{k+1}) \quad (\text{B-4})$$

$$\mathbf{q}_y^{k+1} = \mathbf{q}_y^k + \xi(\mathbf{p}_y^{k+1} - \mathbf{x}^{k+1}) \quad (\text{B-5})$$

$$\mathbf{q}_z^{k+1} = \mathbf{q}_z^k + \xi(\mathbf{p}_z^{k+1} - \nabla_z \mathbf{x}^{k+1}) \quad (\text{B-6})$$

where \mathbf{x}^{k+1} and $\mathbf{p}_x^{k+1}, \mathbf{p}_y^{k+1}, \mathbf{p}_z^{k+1}$ are obtained by solving

$$\begin{aligned} \arg \min_{\mathbf{x}, \mathbf{p}_x, \mathbf{p}_y \in \mathcal{X}, \mathbf{p}_z} & \sum_{i=1}^N \sqrt{|\mathbf{p}_x|_i^2 + |\mathbf{p}_z|_i^2} + \frac{\lambda}{2} \|\mathbf{G}\mathbf{x} - \mathbf{y}\|_2^2 \\ & + \langle \mathbf{q}_x^k, \mathbf{p}_x - \nabla_x \mathbf{x} \rangle + \frac{\xi}{2} \|\mathbf{p}_x - \nabla_x \mathbf{x}\|_2^2 \\ & + \langle \mathbf{q}_y^k, \mathbf{p}_y - \mathbf{x} \rangle + \frac{\xi}{2} \|\mathbf{p}_y - \mathbf{x}\|_2^2 \\ & + \langle \mathbf{q}_z^k, \mathbf{p}_z - \nabla_z \mathbf{x} \rangle + \frac{\xi}{2} \|\mathbf{p}_z - \nabla_z \mathbf{x}\|_2^2, \end{aligned} \quad (\text{B-7})$$

beginning with $\mathbf{p}_x^0 = \mathbf{p}_y^0 = \mathbf{p}_z^0 = \mathbf{0}$.

Equations B-4-B-7 can be simplified by using a change of variables ($\mathbf{q}_x \leftarrow \frac{1}{\xi} \mathbf{q}_x, \mathbf{q}_y \leftarrow \frac{1}{\xi} \mathbf{q}_y, \mathbf{q}_z \leftarrow \frac{1}{\xi} \mathbf{q}_z$) using the fact that for two real vectors \mathbf{a} and \mathbf{b} the following holds:

$$\langle \mathbf{a}, \mathbf{b} \rangle + \frac{\xi}{2} \|\mathbf{b}\|_2^2 = \frac{\xi}{2} \|\mathbf{b} + \frac{1}{\xi} \mathbf{a}\|_2^2 - \frac{\xi}{2} \|\frac{1}{\xi} \mathbf{a}\|_2^2. \quad (\text{B-8})$$

Accordingly,

$$\mathbf{q}_x^{k+1} = \mathbf{q}_x^k + \mathbf{p}_x^{k+1} - \nabla_x \mathbf{x}^{k+1} \quad (\text{B-9})$$

$$\mathbf{q}_y^{k+1} = \mathbf{q}_y^k + \mathbf{p}_y^{k+1} - \mathbf{x}^{k+1} \quad (\text{B-10})$$

$$\mathbf{q}_z^{k+1} = \mathbf{q}_z^k + \mathbf{p}_z^{k+1} - \nabla_z \mathbf{x}^{k+1} \quad (\text{B-11})$$

and

$$\begin{aligned} \arg \min_{\mathbf{x}, \mathbf{p}_x, \mathbf{p}_y \in \mathcal{X}, \mathbf{p}_z} & \sum_{i=1}^N \sqrt{|\mathbf{p}_x|_i^2 + |\mathbf{p}_z|_i^2} + \frac{\lambda}{2} \|\mathbf{G}\mathbf{x} - \mathbf{y}\|_2^2 \\ & + \frac{\xi}{2} \|\mathbf{p}_x - \nabla_x \mathbf{x} + \mathbf{q}_x^k\|_2^2 - \frac{\xi}{2} \|\mathbf{q}_x^k\|_2^2 \\ & + \frac{\xi}{2} \|\mathbf{p}_y - \mathbf{x} + \mathbf{q}_y^k\|_2^2 - \frac{\xi}{2} \|\mathbf{q}_y^k\|_2^2 \\ & + \frac{\xi}{2} \|\mathbf{p}_z - \nabla_z \mathbf{x} + \mathbf{q}_z^k\|_2^2 - \frac{\xi}{2} \|\mathbf{q}_z^k\|_2^2. \end{aligned} \quad (\text{B-12})$$

3) *Alternating minimization.* The basic augmented Lagrangian method minimizes the objective function in equation B-12 (augmented Lagrangian function) jointly over $\mathbf{x}, \mathbf{p}_x, \mathbf{p}_y$, and \mathbf{p}_z , the third trick is to perform this minimization by alternating minimizing with respect to each variable separately (Goldstein and Osher, 2009; Boyd et al., 2010) to arrive at the so-called ADMM.

$$\begin{aligned} \mathbf{x}^{k+1} = \arg \min_{\mathbf{x}} & \frac{\lambda}{2} \|\mathbf{G}\mathbf{x} - \mathbf{y}\|_2^2 + \frac{\xi}{2} \|\mathbf{p}_x^k - \nabla_x \mathbf{x} + \mathbf{q}_x^k\|_2^2 \\ & + \frac{\xi}{2} \|\mathbf{p}_y^k - \mathbf{x} + \mathbf{q}_y^k\|_2^2 + \frac{\xi}{2} \|\mathbf{p}_z^k - \nabla_z \mathbf{x} + \mathbf{q}_z^k\|_2^2. \end{aligned} \quad (\text{B-13})$$

$$\begin{aligned} (\mathbf{p}_x^{k+1}, \mathbf{p}_z^{k+1}) = \arg \min_{\mathbf{p}_x, \mathbf{p}_z} & \sum_{i=1}^N \sqrt{|\mathbf{p}_x|_i^2 + |\mathbf{p}_z|_i^2} \\ & + \frac{\xi}{2} \|\mathbf{p}_x - \nabla_x \mathbf{x}^{k+1} + \mathbf{q}_x^k\|_2^2 \\ & + \frac{\xi}{2} \|\mathbf{p}_z - \nabla_z \mathbf{x}^{k+1} + \mathbf{q}_z^k\|_2^2. \end{aligned} \quad (\text{B-14})$$

$$\mathbf{p}_y^{k+1} = \arg \min_{\mathbf{p}_y \in \mathcal{X}} \frac{\xi}{2} \|\mathbf{p}_y - \mathbf{x}^{k+1} + \mathbf{q}_y^k\|_2^2. \quad (\text{B-15})$$

Subproblem B-13 is an easy-to-solve least-squares problem, which has a closed-form solution obtained by setting the derivative of the objective function with respect to \mathbf{x} equal to zero.

$$\begin{aligned} \mathbf{x}^{k+1} = & [\lambda \mathbf{G}^T \mathbf{G} + \xi \nabla_x^T \nabla_x + \xi \mathbf{I} + \xi \nabla_z^T \nabla_z]^{-1} \\ & [\lambda \mathbf{G}^T \mathbf{y} + \xi \nabla_x^T [\mathbf{p}_x^k + \mathbf{q}_x^k] + \xi [\mathbf{p}_y^k + \mathbf{q}_y^k] + \xi \nabla_z^T [\mathbf{p}_z^k + \mathbf{q}_z^k]]. \end{aligned} \quad (\text{B-16})$$

Subproblem B-14 also has a closed form solution, given by the generalized soft thresholding function (Goldstein and Osher, 2009),

$$\mathbf{p}_x^{k+1} = \max(1 - \frac{1/\xi}{\mathbf{r}}, 0) \circ (\nabla_x \mathbf{x}^{k+1} - \mathbf{q}_x^k), \quad (\text{B-17})$$

and

$$\mathbf{p}_z^{k+1} = \max(1 - \frac{1/\xi}{\mathbf{r}}, 0) \circ (\nabla_z \mathbf{x}^{k+1} - \mathbf{q}_z^k), \quad (\text{B-18})$$

where

$$\mathbf{r} = \sqrt{|\nabla_x \mathbf{x}^{k+1} - \mathbf{q}_x^k|_2^2 + |\nabla_z \mathbf{x}^{k+1} - \mathbf{q}_z^k|_2^2}. \quad (\text{B-19})$$

Subproblem B-15 is a projection operator given by

$$\mathbf{q}^{k+1} = \text{proj}_{\mathcal{X}}(\mathbf{x}^{k+1} - \mathbf{q}_y^k). \quad (\text{B-20})$$

In the case that \mathcal{X} is a box set of form

$$\mathcal{X} = \{\mathbf{x} | \mathbf{x}_{min} \leq \mathbf{x} \leq \mathbf{x}_{max}\}, \quad (\text{B-21})$$

then the projection operator admit a closed form solution

$$\text{proj}_{\mathcal{X}}(\mathbf{x}^{k+1} - \mathbf{q}_y^k) = \min(\max(\mathbf{x}^{k+1} - \mathbf{q}_y^k, \mathbf{x}_{min}), \mathbf{x}_{max}),$$

where \mathbf{x}_{min} and \mathbf{x}_{max} are lower and upper bounds of \mathbf{x} , respectively.

REFERENCES

- Aghamiry, H., A. Gholami, and S. Operto, 2019a, Accurate and efficient wavefield reconstruction in the time domain: *Geophysics*, **85**(2), 1–6.
- , 2019b, ADMM-based multi-parameter wavefield reconstruction inversion in VTI acoustic media with TV regularization: *Geophysical Journal International*, **219**, 1316–1333.
- , 2019c, Compound regularization of Full-Waveform Inversion for imaging piecewise media: *IEEE Transactions on Geoscience and Remote Sensing*, **10.1109/TGRS.2019.2944464**.
- , 2019d, Implementing bound constraints and total-variation regularization in extended full waveform inversion with the alternating direction method of multiplier: application to large contrast media: *Geophysical Journal International*, **218**, 855–872.

- , 2019e, Improving full-waveform inversion by wavefield reconstruction with alternating direction method of multipliers: *Geophysics*, **84(1)**, R139–R162.
- Aki, K. and P. G. Richards, 2002, *Quantitative seismology, theory and methods*, second edition: University Science Books.
- Askan, A., V. Akcelik, J. Bielak, and O. Ghattas, 2007, Full waveform inversion for seismic velocity and anelastic losses in heterogeneous structures: *Bulletin of the Seismological Society of America*, **97**, 1990–2008.
- Asnaashari, A., R. Brossier, S. Garambois, F. Audebert, P. Thore, and J. Virieux, 2013, Regularized seismic full waveform inversion with prior model information: *Geophysics*, **78**, R25–R36.
- Benning, M., F. Knoll, C.-B. Schönlieb, and T. Valkonen, 2015, Preconditioned admm with nonlinear operator constraint: *IFIP Conference on System Modeling and Optimization*, 117–126.
- Bérenger, J.-P., 1994, A perfectly matched layer for absorption of electromagnetic waves: *Journal of Computational Physics*, **114**, 185–200.
- Boyd, S., N. Parikh, E. Chu, B. Peleato, and J. Eckstein, 2010, Distributed optimization and statistical learning via the alternating direction of multipliers: *Foundations and trends in machine learning*, **3**, 1–122.
- Chen, Z., D. Cheng, W. Feng, and T. Wu, 2013, An optimal 9-point finite difference scheme for the Helmholtz equation with PML: *International Journal of Numerical Analysis & Modeling*, **10**.
- Cheng, X., K. Jiao, D. Sun, and D. Vigh, 2016, Multi-parameter estimation with acoustic vertical transverse isotropic full-waveform inversion of surface seismic data: *Interpretation*, **4(4)**, SU1–SU16.
- Combettes, P. L. and J.-C. Pesquet, 2011, Proximal splitting methods in signal processing, *in* Bauschke, H. H., R. S. Burachik, P. L. Combettes, V. Elser, D. R. Luke, and H. Wolkowicz, eds., *Fixed-Point Algorithms for Inverse Problems in Science and Engineering*, volume **49** of *Springer Optimization and Its Applications*, 185–212. Springer New York.
- da Silva, N. and G. Yao, 2017, Wavefield reconstruction inversion with a multiplicative cost function: *Inverse problems*, **34**, 015004.
- da Siva, N. V., G. Yao, and M. Warner, 2019, Semiglobal viscoacoustic full-waveform inversion: *Geophysics*, **84(2)**, R271–R293.
- Dolean, V., P. Jolivet, and F. Nataf, 2015, An introduction to domain decomposition methods - algorithms, theory, and parallel implementation: SIAM.
- Duan, Y. and P. Sava, 2016, Elastic wavefield tomography with physical model constraints: *Geophysics*, **81**, R447–R456.
- Duff, I. S., A. M. Erisman, and J. K. Reid, 1986, *Direct methods for sparse matrices*, second edition: Oxford Science Publications.
- Fu, L. and W. W. Symes, 2017, A discrepancy-based penalty method for extended waveform inversion: *Geophysics*, **R282–R298**, 78–82.
- Futterman, W., 1962, Dispersive body waves: *Journal Geophysical Research*, **67**, 5279–5291.
- Gholami, A., H. Aghamiry, and M. Abbasi, 2018, Constrained nonlinear AVO inversion using Zoeppritz equations: *Geophysics*, **83(3)**, R245–R255.
- Gholami, A. and E. Z. Naeini, 2019, 3D Dix inversion using bound-constrained TV regularization: *Geophysics*, **84**, 1–43.
- Goldstein, T. and S. Osher, 2009, The split Bregman method for L1-regularized problems: *SIAM Journal on Imaging Sciences*, **2**, 323–343.
- Guasch, L., M. Warner, and C. Ravaut, 2019, Adaptive waveform inversion: *Practice: Geophysics*, **84(3)**, R447–R461.
- Hak, B. and W. A. Mulder, 2011, Seismic attenuation imaging with causality: *Geophysical Journal International*, **184**, 439–451.
- He, B., H. Liu, Z. Wang, and X. Yuan, 2014, A strictly contractive peaceman-rachford splitting method for convex programming: *SIAM Journal on Optimization*, **24**, 1011–1040.
- Hestenes, M. R., 1969, Multiplier and gradient methods: *Journal of optimization theory and applications*, **4**, 303–320.
- Hicks, G. J. and R. G. Pratt, 2001, Reflection waveform inversion using local descent methods: estimating attenuation and velocity over a gas-sand deposit: *Geophysics*, **66**, 598–612.
- Kamei, R. and R. G. Pratt, 2008, Waveform tomography strategies for imaging attenuation structure for cross-hole data: 70th Annual International Meeting, EAGE, Expanded Abstracts, F019.
- , 2013, Inversion strategies for visco-acoustic waveform inversion: *Geophysical Journal International*, **194**, 859–894.
- Kolsky, H., 1956, The propagation of stress pulses in viscoelastic solids: *Philosophical Magazine*, **1**, 693–710.
- Kurzmann, A., A. Przebindowska, D. Kohn, and T. Bohlen, 2013, Acoustic full waveform tomography in the presence of attenuation: a sensitivity analysis: *Geophysical Journal International*, **195(2)**, 985–1000.
- Lacasse, M., H. Denli, L. White, V. Gudipati, S. Lee, and S. Tan, 2019, Accounting for heterogeneous attenuation in full-wavefield inversion: Presented at the 81th Annual EAGE Meeting (London) - WS01: Attenuation: Challenges in Modelling and Imaging at the Exploration Scale.
- Malinowski, M., S. Operto, and A. Ribodetti, 2011, High-resolution seismic attenuation imaging from wide-aperture onshore data by visco-acoustic frequency-domain full waveform inversion: *Geophysical Journal International*, **186**, 1179–1204.
- Marfurt, K., 1984, Accuracy of finite-difference and finite-element modeling of the scalar and elastic wave equations: *Geophysics*, **49**, 533–549.
- Métivier, L., A. Allain, R. Brossier, Q. Méridot, E. Oudet,

- and J. Virieux, 2018, Optimal transport for mitigating cycle skipping in full waveform inversion: a graph space transform approach: *Geophysics*, **83**, R515–R540.
- Métivier, L., R. Brossier, S. Operto, and V. J., 2017, Full waveform inversion and the truncated Newton method: *SIAM Review*, **59**, 153–195.
- Métivier, L., R. Brossier, S. Operto, and J. Virieux, 2015, Acoustic multi-parameter FWI for the reconstruction of P-wave velocity, density and attenuation: preconditioned truncated Newton approach: 85th Annual Meeting-New Orleans, Expanded Abstracts, 1198–1203, SEG.
- Mulder, W. A. and B. Hak, 2009, An ambiguity in attenuation scattering imaging: *Geophysical Journal International*, **178**, 1614–1624.
- Munns, J. W., 1985, The Valhall field: a geological overview: *Marine and Petroleum Geology*, **2**, 23–43.
- Nocedal, J. and S. J. Wright, 2006a, *Numerical optimization*: Springer, 2nd edition.
- , 2006b, *Numerical optimization*: Springer, 2nd edition.
- Operto, S., R. Brossier, Y. Gholami, L. Métivier, V. Prieux, A. Ribodetti, and J. Virieux, 2013, A guided tour of multiparameter full waveform inversion for multicomponent data: from theory to practice: The Leading Edge, **Special section Full Waveform Inversion**, 1040–1054.
- Operto, S. and A. Miniussi, 2018, On the role of density and attenuation in 3D multi-parameter visco-acoustic VTI frequency-domain FWI: an OBC case study from the North Sea: *Geophysical Journal International*, **213**, 2037–2059.
- Parikh, N. and S. Boyd, 2013, Proximal algorithms: *Foundations and Trends in Optimization*, **1(3)**, 123–231.
- Peaceman, D. W. and H. H. Rachford, Jr, 1955, The numerical solution of parabolic and elliptic differential equations: *Journal of the Society for industrial and Applied Mathematics*, **3**, 28–41.
- Pratt, R. G., C. Shin, and G. J. Hicks, 1998, Gauss-Newton and full Newton methods in frequency-space seismic waveform inversion: *Geophysical Journal International*, **133**, 341–362.
- Prieux, V., R. Brossier, S. Operto, and J. Virieux, 2013, Multiparameter full waveform inversion of multicomponent OBC data from Valhall. Part 1: imaging compressional wavespeed, density and attenuation: *Geophysical Journal International*, **194**, 1640–1664.
- Ribodetti, A., S. Operto, J. Virieux, G. Lambaré, H.-P. Valéro, and D. Gibert, 2000, Asymptotic viscoacoustic diffraction tomography of ultrasonic laboratory data : a tool for rock properties analysis: *Geophysical Journal International*, **140**, 324–340.
- Rudin, L., S. Osher, and E. Fatemi, 1992, Nonlinear total variation based noise removal algorithms: *Physica D*, **60**, 259–268.
- Stopin, A., R.-E. Plessix, and S. Al Abri, 2014, Multiparameter waveform inversion of a large wide-azimuth low-frequency land data set in Oman: *Geophysics*, **79**, WA69–WA77.
- Stopin, A., R.-E. Plessix, H. Kuehl, V. Goh, and K. Overgaag, 2016, Application of visco-acoustic full waveform inversion for gas cloud imaging and velocity model building: Presented at the 78th EAGE Conference and Exhibition 2016, EAGE.
- Takougang, E. M. T. and A. J. Calvert, 2012, Seismic velocity and attenuation structures of the Queen Charlotte Basin from full-waveform tomography of seismic reflection data: *Geophysics*, **77(3)**, B107–B124.
- Tang, Y., 2009, Target-oriented wave-equation least-squares migration/inversion with phase-encoded hessian: *Geophysics*, **74(6)**, WCA95–WCA107.
- Tarantola, A., 1984, Inversion of seismic reflection data in the acoustic approximation: *Geophysics*, **49**, 1259–1266.
- Toksöz, M. N. and D. H. Johnston, 1981, *Geophysics reprint series, no. 2: Seismic wave attenuation*: Society of exploration geophysicists.
- Toverud, T. and B. Ursin, 2005, Comparison of seismic attenuation models using zero-offset vertical seismic profiling (vsp) data: *Geophysics*, **70**, F17–F25.
- van Leeuwen, T. and F. Herrmann, 2016, A penalty method for PDE-constrained optimization in inverse problems: *Inverse Problems*, **32(1)**, 1–26.
- van Leeuwen, T. and F. J. Herrmann, 2013, Mitigating local minima in full-waveform inversion by expanding the search space: *Geophysical Journal International*, **195(1)**, 661–667.
- Virieux, J. and S. Operto, 2009, An overview of full waveform inversion in exploration geophysics: *Geophysics*, **74**, WCC1–WCC26.
- Warner, M. and L. Guasch, 2016, Adaptive waveform inversion: Theory: *Geophysics*, **81**, R429–R445.
- Yang, J., Y. Liu, and L. Dong, 2016, Simultaneous estimation of velocity and density in acoustic multiparameter full-waveform inversion using an improved scattering-integral approach: *Geophysics*, **81**, R399–R415.
- Yang, J.-Z., Y.-Z. Liu, and L.-G. Dong, 2014, A multiparameter full waveform strategy for acoustic media with variable density: *Chinese Journal of Geophysics*, **57**, 628–643.

Algorithm 1 Viscoacoustic Wavefield Inversion with Bound Constrained TV Regularization. Lines 4 to 6 are the primal subproblems for wavefield reconstruction and parameter estimation. Lines 7 to 12 are primal subproblems for auxiliary variables introduced to implement nonsmooth regularizations and bound constraints (Appendix B). Lines 13 to 20 are the dual subproblems solved with gradient ascent steps.

- 1: Begin with $k = 0$, an initial squared slowness \mathbf{m}^0 , and attenuation $\boldsymbol{\alpha}^0$,
 - 2: Set to zero the values of \mathbf{d}^0 , \mathbf{b}^0 , $\mathbf{p}_{x,m}^0$, $\mathbf{p}_{y,m}^0$, $\mathbf{p}_{z,m}^0$, $\mathbf{p}_{x,\alpha}^0$, $\mathbf{p}_{y,\alpha}^0$, $\mathbf{p}_{z,\alpha}^0$, $\mathbf{q}_{x,m}^0$, $\mathbf{q}_{y,m}^0$, $\mathbf{q}_{z,m}^0$, $\mathbf{q}_{x,\alpha}^0$, $\mathbf{q}_{y,\alpha}^0$, $\mathbf{q}_{z,\alpha}^0$,
 - 3: **while** convergence criteria not satisfied **do**
 - 4: $\mathbf{u}^{k+1} = \left[\lambda \mathbf{A}^T \mathbf{A} + \gamma \mathbf{P}^T \mathbf{P} \right]^{-1} \left[\lambda \mathbf{A}^T [\mathbf{b}^k + \mathbf{b}] + \gamma \mathbf{P}^T [\mathbf{d}^k + \mathbf{d}] \right]$
 - 5: $\mathbf{m}^{k+1} = \left[\lambda \mathbf{L}^T \mathbf{L} + \xi_m \nabla_x^T \nabla_x + \xi_m \mathbf{I} + \xi_m \nabla_z^T \nabla_z \right]^{-1} \left[\lambda \mathbf{L}^T \mathbf{y}^k + \xi_m \nabla_x^T [\mathbf{p}_{x,m}^k + \mathbf{q}_{x,m}^k] + \xi_m [\mathbf{p}_{y,m}^k + \mathbf{q}_{y,m}^k] + \xi_m \nabla_z^T [\mathbf{p}_{z,m}^k + \mathbf{q}_{z,m}^k] \right]$
 - 6: $\boldsymbol{\alpha}^{k+1} = \left[\lambda \mathbf{H}^T \mathbf{H} + \xi_\alpha \nabla_x^T \nabla_x + \xi_\alpha \mathbf{I} + \xi_\alpha \nabla_z^T \nabla_z \right]^{-1} \left[\lambda \mathbf{H}^T \mathbf{h}^k + \xi_\alpha \nabla_x^T [\mathbf{p}_{x,\alpha}^k + \mathbf{q}_{x,\alpha}^k] + \xi_\alpha [\mathbf{p}_{y,\alpha}^k + \mathbf{q}_{y,\alpha}^k] + \xi_\alpha \nabla_z^T [\mathbf{p}_{z,\alpha}^k + \mathbf{q}_{z,\alpha}^k] \right]$
 - 7: $\mathbf{p}_{x,m}^{k+1} = \max\left(1 - \frac{\mu/\xi_m}{\sqrt{|\nabla_x \mathbf{m}^{k+1} - \mathbf{q}_{x,m}^k|^2 + |\nabla_z \mathbf{m}^{k+1} - \mathbf{q}_{z,m}^k|^2}}, 0\right) \circ (\nabla_x \mathbf{m}^{k+1} - \mathbf{q}_{x,m}^k)$
 - 8: $\mathbf{p}_{y,m}^{k+1} = \text{proj}_{\mathcal{M}}(\mathbf{m}^{k+1} - \mathbf{q}_{y,m}^k)$
 - 9: $\mathbf{p}_{z,m}^{k+1} = \max\left(1 - \frac{\mu/\xi_m}{\sqrt{|\nabla_x \mathbf{m}^{k+1} - \mathbf{q}_{x,m}^k|^2 + |\nabla_z \mathbf{m}^{k+1} - \mathbf{q}_{z,m}^k|^2}}, 0\right) \circ (\nabla_z \mathbf{m}^{k+1} - \mathbf{q}_{z,m}^k)$
 - 10: $\mathbf{p}_{x,\alpha}^{k+1} = \max\left(1 - \frac{\nu/\xi_\alpha}{\sqrt{|\nabla_x \boldsymbol{\alpha}^{k+1} - \mathbf{q}_{x,\alpha}^k|^2 + |\nabla_z \boldsymbol{\alpha}^{k+1} - \mathbf{q}_{z,\alpha}^k|^2}}, 0\right) \circ (\nabla_x \boldsymbol{\alpha}^{k+1} - \mathbf{q}_{x,\alpha}^k)$
 - 11: $\mathbf{p}_{y,\alpha}^{k+1} = \text{proj}_{\mathcal{A}}(\boldsymbol{\alpha}^{k+1} - \mathbf{q}_{y,\alpha}^k)$
 - 12: $\mathbf{p}_{z,\alpha}^{k+1} = \max\left(1 - \frac{\nu/\xi_\alpha}{\sqrt{|\nabla_x \boldsymbol{\alpha}^{k+1} - \mathbf{q}_{x,\alpha}^k|^2 + |\nabla_z \boldsymbol{\alpha}^{k+1} - \mathbf{q}_{z,\alpha}^k|^2}}, 0\right) \circ (\nabla_z \boldsymbol{\alpha}^{k+1} - \mathbf{q}_{z,\alpha}^k)$
 - 13: $\mathbf{q}_{x,m}^{k+1} = \mathbf{q}_{x,m}^k + \mathbf{p}_{x,m}^{k+1} - \nabla_x \mathbf{m}^{k+1}$
 - 14: $\mathbf{q}_{y,m}^{k+1} = \mathbf{q}_{y,m}^k + \mathbf{p}_{y,m}^{k+1} - \mathbf{m}^{k+1}$
 - 15: $\mathbf{q}_{z,m}^{k+1} = \mathbf{q}_{z,m}^k + \mathbf{p}_{z,m}^{k+1} - \nabla_z \mathbf{m}^{k+1}$
 - 16: $\mathbf{q}_{x,\alpha}^{k+1} = \mathbf{q}_{x,\alpha}^k + \mathbf{p}_{x,\alpha}^{k+1} - \nabla_x \boldsymbol{\alpha}^{k+1}$
 - 17: $\mathbf{q}_{y,\alpha}^{k+1} = \mathbf{q}_{y,\alpha}^k + \mathbf{p}_{y,\alpha}^{k+1} - \boldsymbol{\alpha}^{k+1}$
 - 18: $\mathbf{q}_{z,\alpha}^{k+1} = \mathbf{q}_{z,\alpha}^k + \mathbf{p}_{z,\alpha}^{k+1} - \nabla_z \boldsymbol{\alpha}^{k+1}$
 - 19: $\mathbf{b}^{k+1} = \mathbf{b}^k + \mathbf{b} - \mathbf{A}(\mathbf{m}^{k+1}, \boldsymbol{\alpha}^{k+1})\mathbf{u}^{k+1}$
 - 20: $\mathbf{d}^{k+1} = \mathbf{d}^k + \mathbf{d} - \mathbf{P}\mathbf{u}^{k+1}$
 - 21: $k = k + 1$
 - 22: **end while**
-